An implicit level set method for modeling hydraulically driven fractures

Anthony Peirce [a,*], Emmanuel Detournay [b]

[a] *University of British Columbia, Department of Mathematics, Vancouver, BC, Canada V6T 1Z2*
[b] *University of Minnesota, Department of Civil Engineering, Minneapolis, MN 55455, USA*

Dedicated to J.R.A. Pearson, FRS, who, 15 years ago, recognized that incorporating the relevant tip asymptotics
in hydraulic fracture simulators is critical for the accuracy and stability of the algorithms.

Abstract

We describe a novel implicit level set algorithm to locate the free boundary for a propagating hydraulic fracture. A number of characteristics of the governing equations for hydraulic fractures and their coupling present considerable challenges for numerical modeling, namely: the degenerate lubrication equation; the hypersingular elastic integral equation; the indeterminate form of the velocity of the unknown fracture front, which precludes the implementation of established front evolution strategies that require an explicit velocity field; and the computationally prohibitive cost of resolving all the length scales. An implicit algorithm is also necessary for the efficient solution of the stiff evolution equations that involve fully populated matrices associated with the coupled non-local elasticity and degenerate lubrication equations. The implicit level set algorithm that we propose exploits the local tip asymptotic behavior, applicable at the computational length scale, in order to locate the free boundary. Local inversion of this tip asymptotic relation yields the boundary values for the Eikonal equation, whose solution gives the fracture front location as well as the front velocity field. The efficacy of the algorithm is tested by comparing the level set solution to analytic solutions for hydraulic fractures propagating in a number of distinct regimes. The level set algorithm is shown to resolve the free boundary problem with first order accuracy. Further it captures the field variables, such as the fracture width, with the first order accuracy that is consistent with the piecewise constant discretization that is used.
© 2008 Elsevier B.V. All rights reserved.

Keywords: Fracture mechanics; Level set; Moving front; Hydraulic fracture

1. Introduction

Fluid-driven fractures are a class of tensile fractures that propagate in compressively prestressed solid media due to internal pressurization by an injected viscous fluid. There are numerous examples of hydraulic fractures (HF) that occur both in natural geological processes as well as in geo-engineering. At the geological scale, these fractures occur as kilometers-long vertical dikes that bring magma from deep underground chambers to the earth's surface [1–3]; they also occur as horizontal fractures that divert magma from dikes to form so-called sills that are sub-parallel to the earth's surface due, in part, to favorable *in situ* stress fields [4,5]. At an engineering scale, hydraulic fractures can propagate in dams [6,7], sometimes causing the failure of the whole structure [8]. However, hydraulic fractures are also engineered for a variety of industrial applications including: remediation projects in contaminated soils [9–11]; waste disposal [12,13]; excavation of hard rocks [14]; preconditioning and cave inducement in mining [15,16], and most commonly for the stimulation of hydrocarbon-bearing rock strata to increase production in oil and gas wells [17–19]. To minimize the energy expended during propagation, hydraulic fractures typically develop in a plane that is perpendicular to the direction of the minimum principal *in situ* compressive stress.

---

* Corresponding author.
E-mail addresses: peirce@math.ubc.ca (A. Peirce), detou001@umn.edu
(E. Detournay).

The numerical simulation of fluid-driven fractures remains a particularly challenging computational problem, despite significant progress made since the first algorithms were developed in the 1970s [20,21]. The challenge encountered in devising stable and robust algorithms stems from three distinct issues that arise from the particular structure of this problem. Firstly, the lubrication equation, governing the flow of viscous fluid in the fracture, involves a degenerate non-linear partial differential equation. The coefficients in the principal part of this equation vanish as a power of the unknown fracture width similar to the degenerate porous medium equations, or, for a non-Newtonian fluid, these coefficients may vanish with powers of the pressure gradient similar to the p-Laplace equations. This non-linear degeneracy poses considerable challenges for numerical modeling – for example near the fracture tip, where the aperture tends to zero. Secondly, the elasticity equation, which expresses the balance of forces between the fluid pressure, the *in situ* stresses, and the linear elastic response of the rock mass, involves a boundary integral equation with a hypersingular kernel. Thirdly, the footprint of the fracture and its encompassing boundary is also unknown. The resolution of this free boundary problem requires that an additional growth condition be specified. This condition, which comes from linear elastic fracture mechanics (LEFM), specifies that the stress intensity factor along the perimeter of the fracture should be in limit equilibrium with a material parameter known as the toughness. The stress intensity factor is a functional of the fracture opening and geometry, while the toughness is related to the amount of energy that is required to break the rock. Established methods for free boundary evolution, such as the front tracking and the volume-of-fluid methods both need an accurate front velocity, while the level set method requires the determination of an extension velocity field in addition to an accurate front velocity. As with other degenerate diffusion problems [22,23], the HF front velocity can only be determined by evaluating an indeterminate limit involving a product of the vanishing fracture width and the pressure gradient, which tends to infinity at the front. Evaluating this indeterminate limit numerically poses a considerable challenge.

The degenerate non-linear lubrication PDE, the hypersingular non-local elasticity operator, and the fracture propagation criterion combine to yield a multi-scale structure of the solution near the fracture tip [24–27]. This multi-scale solution structure results from the competing physical processes that manifest themselves at different length and time scales. For example, the viscous energy dissipation associated with driving the fluid through the fracture competes with the energy required to break the rock. The multi-scale tip asymptotics has to be properly captured at the discretization length scale used in the numerical scheme to yield an accurate prediction of the fracture evolution [28,29]. In particular, there are conditions – actually prevalent in hydraulic fracturing treatments – under which the classical square root asymptote of linear elastic fracture

mechanics exists at such a small scale that it cannot be resolved at the discretization length used to conduct the computations. Under these conditions, which correspond to the viscosity-dominated regime of fracture propagation, significant errors in the prediction of the fracture dimension and width result from imposing an asymptotic behavior that is not relevant at the grid size used to carry out the computations. The recent progress in the development of these matched asymptotic solutions in the vicinity of the fracture tip presents the opportunity for substantially improving the accuracy of the numerical solutions by employing the appropriate asymptotic behavior in the representation of the numerical solution as well as in the location of the free boundary. Indeed, the objective of this paper is to provide a methodology that can exploit these asymptotic solutions in an algorithm that yields accurate numerical results with relatively few computational resources.

While the above three attributes each present difficulties for numerical computation, their combination in the coupled equations conspire to substantially complicate the numerical solution. Due to its sedimentary genesis, the elastic rock mass is typically assumed to comprise bonded, homogeneous layers. For such a layered medium, assembling the Green's function matrix for the discretization of the integral equation involves the solution of a new three-dimensional boundary value problem for each *additional* degree of freedom. This constraint makes it impracticable to use a Lagrangian moving mesh algorithm to capture the rapid variation of the solution that is to be expected in the vicinity of the fracture front. By exploiting the translational invariance of the integral operator parallel to the layers, an Eulerian approach involving rectangular elements yields considerable savings in memory requirements and CPU resources [30–32]. Although we do not consider layered problems in this paper, we do adopt an Eulerian rectangular mesh in the discretization of the problem in order to explore the feasibility of this approach.

When discretized in space, the coupled system of non-linear integro-partial differential equations reduces to a stiff system of ordinary differential equations for which explicit time stepping involves a CFL condition of the form $\Delta t = O(\Delta x^3)$ [33]. Since evaluation of the discrete integral operator involves $O(N^2)$ operations, this time step restriction makes explicit time stepping an extremely computationally intensive option. For a layered elastic material, the FFT can be used to reduce this count to $O(N^{\frac{3}{2}} \log N)$ operations, while jump discontinuities in the field variables across layer interfaces make the implementation of a fast multipole algorithm difficult. As a result, implicit time stepping is required to solve for the field variables comprising the fracture width and the fluid pressure, while an implicit algorithm is also required to locate the free boundary. This paper proposes a novel implicit front location algorithm suitable for the propagation of hydraulic fractures by a level set method [34], which involves the solution of the Eikonal equation by the fast marching method (FMM)

[35,36] combined with the tip asymptotic solutions mentioned above.

A number of approaches have been used to solve the HF free boundary problem. Front tracking has been combined with a Lagrangian moving mesh approach [20,21] in which the fracture is assumed to grow until the stress intensity matches the fracture toughness. This approach is not appropriate, for example, when the length scale on which the square root behavior associated with the fracture toughness is much smaller than that of the local mesh size. Assuming an Eulerian mesh with rectangular elements, front tracking [32] and adapted VOF methods with simplified boundary conditions [37] have been used to locate the free boundary for fractures propagating in a viscosity-dominated regime. These techniques are restricted in their application to a single physical process and are certainly not able to model a transition from one propagation regime to another.

On the other hand, FMM level set methods have been used in conjunction with the extended finite element method (xFEM) to model the propagation of fractures [38,39]. These papers consider the growth of "dry cracks" due to the application of a pulsating tensile stress field. The steps in this procedure are as follows: (1) the signed distance function T is calculated by solving the Eikonal equation $F|\nabla T| = 1$ with the speed function F set to unity and the boundary condition $T(x, y) = 0$ imposed along the current fracture front; (2) the Paris growth law [40] is used to calculate a normal velocity field F for the fracture front (in pseudo-time); (3) using the signed distance function $T(x, y)$ and the value of F on the front, the extension velocity field F_{ext} is constructed; (4) using this extension velocity field the Eikonal equation $F_{\text{ext}}|\nabla T_{\text{ext}}| = 1$ is used to construct the crossing-time map from which a new front position is determined, and the process is repeated. To implement Paris' law, the stress intensity factor has to be evaluated for the current fracture footprint at considerable computational expense. In the HF context this approach will not work since determining the front velocity involves the evaluation of an indeterminate form.

The implicit level set algorithm we propose relies on a tip asymptotic relation of the form

$$w \overset{s \ll 1}{\sim} W(s; V, E', \mu', K', C') \tag{1}$$

to provide the information about the location of the fracture front. Here w is the fracture opening, s is the distance from the fracture front and V is the local front velocity, while E', μ', K', and C' are material parameters, and W is a monotonically increasing function of s. Since it is important that the algorithm be able to locate the fracture front implicitly, the following iterative procedure is adopted. Given the current fracture footprint at time $t - \Delta t$, we search for the location of the fracture front at time t. With the increased time and the additional fluid that has been injected into the fracture over the time step Δt, the coupled elasticity and lubrication equations are solved to determine the frac-

ture width w and the corresponding fluid pressure p_{f}. The asymptotic relation (1) is inverted for the band of elements that are closest to the current fracture front and which fall entirely within the fracture perimeter. By setting $T(x, y) = -s$ for each of these band elements and solving the Eikonal equation $|\nabla T| = 1$, we obtain an estimate of the desired zero crossing-time map $T(x, y) = 0$, from which the new front location can now be determined. With this new fracture footprint, the coupled elasticity and lubrication equations are solved to determine the corresponding width and fluid pressures and the process is repeated until the fracture footprint has converged. The time is then advanced, bringing more fluid into the fracture, and the above sequence of front location steps is repeated. This algorithm is amenable to implicit implementation and provides a direct calculation of the crossing-time map without requiring the normal front velocity field or its extension field. Therefore, this procedure avoids having to estimate the normal front velocity from an indeterminate limit involving divided differences of the pressure field. Indeed, for those asymptotic relations (1) in which the front velocity V appears explicitly, it is possible to use the implicit level set formulation to determine the local front velocity as part of the process of inverting (1). Updating the signed distance function is done naturally at the beginning of each iteration by using the asymptotic relation (1) and no extension velocity field is required. It is interesting to note that for dry cracks, which are probably the most commonly modeled fracture propagation process, the asymptotic expansion is equivalent to the statement that the stress intensity function is in limit equilibrium with the fracture toughness, which is precisely the same as the fracture growth criterion used in [39]. In the numerical examples, we demonstrate that the implicit level set algorithm can also be used to model the propagation of dry cracks.

In Section 2, we describe the governing equations and the appropriate scaling for a hydraulic fracture. In Section 3, we briefly summarize the tip asymptotic solutions that are central to the successful implementation of the novel implicit level set algorithm to capture the free boundary. In Section 4, we describe the discretization of the governing equations: for the integral operator we use piecewise constant displacement discontinuities; for the lubrication equation we use a finite volume approach for interior elements and weak form tip asymptotics to account for the fluid volume stored in tip elements, while exact integration of the sink terms is used to determine the fluid leaked from tip elements. We also describe a mixed-variable formulation of the discrete equations that are required to determine the unknown channel widths and tip pressures. In Section 5, we describe the details of the implicit level set method: for a number of important physical cases we invert the tip asymptotic relations to determine the boundary conditions for the Eikonal equation, whose solution is then used to locate the fracture front. In Section 6, we provide a number of comparisons between the numerical solution proposed in this paper and radially symmetric analytic

solutions. A number of distinct propagation regimes are considered in order to demonstrate the versatility of the new method: (1) a radially symmetric fracture subject to a pressure field that is constant in space; (2) a radially symmetric fracture propagating in a storage-toughness-dominated regime; (3) in a storage-viscosity-dominated regime we consider both a radially symmetric fracture as well as a fracture propagating in a symmetry-breaking *in situ* stress field; (4) a radially symmetric fracture propagating in a viscosity-dominated regime with significant leak-off.

In Appendix A, we provide details of the tip volume calculations required to implement the new implicit level set algorithm. In Appendix B, we demonstrate that, for a regular fracture front, the governing equations reduce, in the near-tip asymptotic limit, to those for a one-dimensional crack propagating under conditions of plane strain. In Appendix C, we compile analytic solutions for a radially symmetric fracture subject to a constant pressure field as well as HF that are propagating in the following three specific regimes: storage-toughness-dominated, storage-viscosity-dominated, leak-off-viscosity dominated. In Appendix D, we provide the viscosity-toughness scaling suitable for the analysis of hydraulic fractures that propagate in a regime in which toughness and viscosity are the dominant physical processes while leak-off is sub-dominant.

2. Mathematical model

2.1. Assumptions

The equations governing the propagation of a hydraulic fracture in a reservoir have to account for the dominant physical processes that take place during the treatment: deformation of the rock, creation of new fracture surface, flow of fracturing fluid within the crack, leak-off of fracturing fluid into the reservoir, and formation of a cake by particles in the fluid. Besides the standard assumptions regarding the applicability of LEFM and lubrication theory, we make a series of simplifications that can readily be justified for the purposes of this contribution: (i) the rock is homogeneous (having uniform values of toughness K_{Ic}, Young's modulus E, and Poisson's ratio v), (ii) the fracturing fluid is incompressible and Newtonian (having a viscosity μ), (iii) the fracture is always in limit equilibrium, (iv) leak-off of the fracturing fluid into the formation is modeled according to Carter's theory [41], which is characterized by the Carter leak-off coefficient C_L, which is assumed to be constant, (v) gravity is neglected in the lubrication equation, and (vi) the fluid front coincides with the crack front, because the lag between the two fronts is negligible under typical high confinement conditions encountered in reservoir stimulation [24,42].

The assumption that K_{Ic} and μ are homogeneous can be relaxed without any significant changes to the model. The assumption that E and v are homogeneous is not trivial to relax (see for example [30–32]), however we do assume a rectangular Eulerian grid on which an efficient multi-

layer algorithm can be implemented without revising the algorithm presented in this paper. This can be achieved by merely replacing the Green's function matrix elements for a homogeneous elastic medium by those for a layered elastic medium.

2.2. Mathematical formulation

The solution of the hydraulic fracture problem comprises the fracture aperture $w(x,y,t)$, the fluid pressure $p_f(x,y,t)$, the flux $\mathbf{q}(x,y,t)$, and the position of the front $C(t)$, where t denotes the time and x, y are the coordinates in a system of axes referenced to the injection point, see Fig. 1. The solution depends on the injection rate $Q(t)$, the far-field compressive stress $\sigma(x,y)$ perpendicular to the fracture plane (a known function of position), and the four material parameters μ', C', E', K' defined as

$$\mu' = 12\mu, \quad C' = 2C_L, \quad E' = \frac{E}{1-v^2}, \quad K' = 4\left(\frac{2}{\pi}\right)^{1/2} K_{Ic}. \quad (2)$$

Here E' is the plane strain modulus and the alternate viscosity μ', toughness K', and leak-off coefficient C' are introduced to keep equations uncluttered by numerical factors. The front $C(t)$, and the field quantities $w(x,y,t)$, $p_f(x,y,t)$, and $\mathbf{q}(x,y,t)$ are governed by a set of equations arising from linear elastic fracture mechanics, lubrication theory, filtration theory, and the associated boundary conditions.

2.2.1. Elasticity

In view of the homogeneous nature of the infinite medium, the elasticity equations, relating the displacement and stress fields in the solid, can be condensed into a hypersingular integral equation between the fracture aperture w and the fluid pressure p_f [43,44]

$$p = p_f - \sigma = -\frac{E'}{8\pi} \int_{A(t)} \frac{w(x',y',t)\,dA(x',y')}{[(x'-x)^2 + (y'-y)^2]^{3/2}}, \quad (3)$$

where $A(t)$ denotes the fracture footprint (enclosed by the crack front $C(t)$ and having a characteristic dimension $L(t)$), and p is the net pressure.

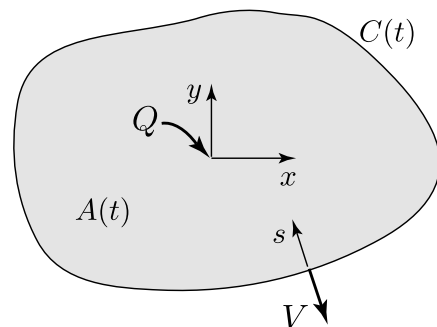
Fig. 1. Sketch of a planar fracture.

2.2.2. Lubrication

The lubrication equations consist of Poiseuille's law

$$\mathbf{q} = -\frac{w^3}{\mu'}\nabla p_f \tag{4}$$

and the continuity equation

$$\frac{\partial w}{\partial t} + g + \nabla \cdot \mathbf{q} = Q(t)\delta(x,y), \tag{5}$$

with the leak-off rate $g(x,y,t)$ given by

$$g = \frac{C'H(t - t_0(x,y))}{\sqrt{t - t_0(x,y)}}, \tag{6}$$

where t_0 denotes the time that the point (x,y) within the fracture was first exposed to fluid and H is the Heavyside function. Eqs. (4) and (5) can be combined to yield Reynolds' lubrication equation

$$\frac{\partial w}{\partial t} + g = \frac{1}{\mu'}\nabla \cdot (w^3\nabla p_f) + Q(t)\delta(x,y). \tag{7}$$

It should be noted that $t_0(x,y)$ is not known *a priori* but depends on the location of the unknown fracture front over the evolution of the fracture. Thus, since the history term $g(x,y,t)$ involves delays, which depend on the unknowns of the problem, the lubrication Eq. (7) is classified as a delay partial differential equation.

2.2.3. Boundary conditions at the moving front $C(t)$

The boundary conditions at the front $C(t)$ are deduced from the propagation criterion and a zero flux condition. Assuming that the fracture is always in limit equilibrium and that a limiting condition is reached everywhere along the front, implies that the fracture aperture in the immediate vicinity of the front is given by

$$w \sim \frac{K'}{E'}s^{1/2} \tag{8}$$

where s denotes the distance from the crack front $C(t)$ (with the s-axis directed inwards). The form of this condition is a classical result from LEFM [45].

The second condition simply expresses a zero flux boundary condition at the fracture tip

$$\lim_{s \to 0} w^3\frac{\partial p_f}{\partial s} = 0. \tag{9}$$

We note that the pressure gradient becomes infinite as $s \to 0$ according to both Eqs. (3) and (7), since $w \to 0$ as $s \to 0$. Unlike a classical Stefan boundary condition at a moving front, where the front velocity is given in terms of quantities having a definite limit at the front, the front velocity has to be extracted from an asymptotic analysis of the non-linear system of Eqs. (3)–(9). In the particular case of an impermeable medium, the front velocity V is equal to the average fluid velocity as $s \to 0$

$$V = \frac{1}{\mu'}\lim_{s \to \circ} w^2\frac{\partial p_f}{\partial s}, \quad \text{if } C' = 0, \tag{10}$$

which shows that V is the limit of an indeterminate form when $C' = 0$. If $C' > 0$ then V is the limit of another indeterminate form. The above discussion makes it clear that velocity-based front location algorithms face a serious challenge due to the need to evaluate large pressure gradients and large leak-off velocities in order to estimate the front velocity.

2.3. Scaling

2.3.1. Multiple time scales

The system of Eqs. (3) and (7)–(9) is closed and can, in principle, be solved to determine the evolution of a hydraulic fracture, given appropriate initial conditions. Before discussing the solution of this system of equations as well as its behavior in the tip region, it is convenient to scale the problem.

We now summarize the scaling laws for the special case of a penny-shaped fracture (also referred to as a radial or axisymmetric fracture) driven by a fluid injected at a constant rate [46], as these laws are the key to understanding the different regimes of propagation.

Propagation of a hydraulic fracture with zero lag is governed by two competing dissipative processes associated with fluid viscosity and solid toughness, respectively, and two competing components of the fluid balance associated with fluid storage in the fracture and fluid storage in the surrounding rock (leak-off). Consequently, limiting propagation regimes can be associated with the dominance of one of the two dissipative processes and/or the dominance of one of the two fluid storage mechanisms. Thus, we can identify *four primary asymptotic regimes* of hydraulic fracture propagation (with zero lag) where one of the two dissipative mechanisms and one of the two fluid storage components vanish: storage-viscosity (M), storage-toughness (K), leak-off-viscosity $(\widetilde{M})$, and leak-off-toughness $(\widetilde{K})$ dominated regimes. For example, in the storage-viscosity-dominated regime (M), fluid leak-off is negligible compared to fluid storage in the fracture and the energy expended in fracturing the rock is negligible compared to viscous dissipation. The solution in the storage-viscosity-dominated limiting regime is given by the zero-toughness, zero-leak-off solution $(K' = C' = 0)$.

Consider the general scaling of a finite fracture which hinges on defining the dimensionless crack opening $\Omega(\rho;\mathcal{P}_1,\mathcal{P}_2)$, net pressure $\Pi(\rho;\mathcal{P}_1,\mathcal{P}_2)$, and fracture radius $\gamma(\mathcal{P}_1,\mathcal{P}_2)$ as [47,46]

$$w = \varepsilon L\Omega, \quad p = \varepsilon E', \quad R = \gamma L. \tag{11}$$

With these definitions, we have introduced the scaled coordinate $\rho = r/R(t)$ $(0 \leqslant \rho \leqslant 1)$, a small parameter $\varepsilon(t)$, a length scale $L(t)$ of the same order of magnitude as the fracture length $R(t)$. In addition, we define two dimensionless evolution parameters $\mathcal{P}_1(t)$ and $\mathcal{P}_2(t)$, which depend monotonically on t.

Four different scalings can be defined in connection to the four primary limiting cases introduced earlier. These

Table 1
Small parameter ε, length scale L for the two storage scalings (viscosity and toughness) and the two leak-off scalings (viscosity and toughness)

Scaling	ε	L	$\mathscr{P}_1$	$\mathscr{P}_2$
Storage/viscosity (M)	$(\frac{\mu'}{E't})^{1/3}$	$(\frac{E'Q_0^3t^4}{\mu'})^{1/9}$	$\mathscr{K}_m = (\frac{K'^{18}t^2}{\mu'^5E'^{13}Q_0^3})^{\frac{1}{18}}$	$\mathscr{C}_m = (\frac{C'^{18}E'^4t^7}{\mu'^4Q_0^6})^{\frac{1}{18}}$
Storage/toughness (K)	$(\frac{K'^6}{E'^6Q_0t})^{1/5}$	$(\frac{E'Q_0t}{K'})^{2/5}$	$\mathscr{M}_k = (\frac{\mu'^5Q_0^3E'^{13}}{K'^{18}t^2})^{\frac{1}{5}}$	$\mathscr{C}_k = (\frac{C'^{10}E'^8t^3}{K'^8Q_0^2})^{\frac{1}{10}}$
Leak-off/viscosity ($\tilde{M}$)	$(\frac{\mu'^4C'^6}{E'^4Q_0^2t})^{\frac{1}{16}}$	$(\frac{Q_0^2t}{C'^2})^{1/4}$	$\mathscr{K}_{\tilde{m}} = (\frac{K'^{16}t}{E'^{12}\mu'^4C'^2Q_0^2})^{\frac{1}{16}}$	$\mathscr{S}_{\tilde{m}} = (\frac{C'^8t}{E'^4C'^{18}t^7})^{\frac{1}{16}}$
Leak-off/toughness ($\tilde{K}$)	$(\frac{K'^8C'^2}{E'^8Q_0^2t})^{1/8}$	$(\frac{Q_0^2t}{C'^2})^{1/4}$	$\mathscr{M}_{\tilde{k}} = (\frac{\mu'^4E'^{12}C'^2Q_0^2}{K'^{16}t})^{\frac{1}{4}}$	$\mathscr{S}_{\tilde{k}} = (\frac{K'^8Q_0}{E'^8C'^{10}t^3})^{\frac{1}{8}}$

Parameters $\mathscr{P}_1$ and $\mathscr{P}_2$ for the two storage scalings (viscosity and toughness) and the two leak-off scalings (viscosity and toughness).

scalings yield power law dependence of L, ε, $\mathscr{P}_1$, and $\mathscr{P}_2$ on time t; i.e. $L \sim t^\alpha$, $\varepsilon \sim t^\delta$, $\mathscr{P}_1 \sim t^{\beta_1}$, $\mathscr{P}_2 \sim t^{\beta_2}$, see Table 1 for the case of a radial fracture. Furthermore, the evolution parameters can take either the meaning of a toughness ($\mathscr{K}_m, \mathscr{K}_{\tilde{m}}$), or a viscosity ($\mathscr{M}_k, \mathscr{M}_{\tilde{k}}$), or a storage ($\mathscr{S}_{\tilde{m}}, \mathscr{S}_{\tilde{k}}$), or a leak-off coefficient ($\mathscr{C}_m, \mathscr{C}_k$). These solution regimes can be conceptualized in a rectangular phase diagram $MK\tilde{K}\tilde{M}$ shown in Fig. 2. For each of the *four primary regimes* ($M, K, \tilde{M}$, and $\tilde{K}$) of hydraulic fracture propagation, corresponding to the vertices of the diagram, both $\mathscr{P}_1$ and $\mathscr{P}_2$ for that particular scaling are zero. For example, at the M-vertex, only viscous dissipation takes place and all the injected fluid is contained in the fracture (so that $\mathscr{K}_m = 0$ and $\mathscr{C}_m = 0$, see Table 1). The similarity solution for each primary regime has the important property that it evolves with time t according to a power law. In particular, the fracture radius R evolves in these regimes according to $R \sim t^\alpha$ where the exponent α depends on the regime of propagation: $\alpha = 4/9, 2/5, 1/4, 1/4$ in the M-, K-, $\tilde{M}$-, $\tilde{K}$-regimes, respectively.

The regime of propagation evolves with time, since the parameters $\mathscr{M}$, $\mathscr{K}$, $\mathscr{C}$ and $\mathscr{S}$ depend on t. With respect to the evolution of the solution in time, it is useful to locate the position of the state point in the $MK\tilde{K}\tilde{M}$ space in terms of the dimensionless times $\tau_{mk} = t/t_{mk}$, $\tau_{m\tilde{m}} = t/t_{m\tilde{m}}$, where the time scales are defined as

$$t_{mk} = \left(\frac{\mu'^5E'^{13}Q_0^3}{K'^{18}}\right)^{1/2}, \quad t_{m\tilde{m}} = \left(\frac{\mu'^4Q_0^6}{E'^4C'^{18}}\right)^{1/7}. \quad (12)$$

Indeed, the parameters $\mathscr{M}$, $\mathscr{K}$, $\mathscr{C}$ and $\mathscr{S}$ can be simply expressed in terms of these times according to

$$\mathscr{K}_m = \mathscr{M}_k^{-5/18} = \tau_{mk}^{1/9}, \quad \mathscr{C}_m = \mathscr{S}_{\tilde{m}}^{-8/9} = \tau_{m\tilde{m}}^{7/18} \quad (13)$$

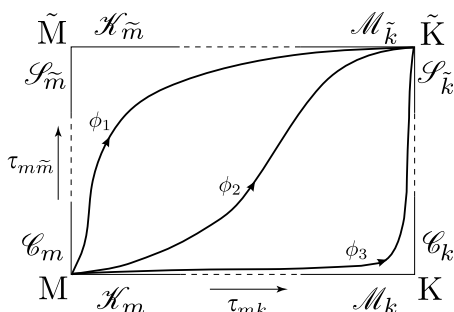Fig. 2. $MK\tilde{K}\tilde{M}$ parameter space [46].

and, therefore, the dimensionless times τ's define the evolution of the solution along the respective edges of the rectangular space $MK\tilde{K}\tilde{M}$. Furthermore, the evolution of the solution regime in the $MK\tilde{K}\tilde{M}$ space takes place along a trajectory corresponding to a constant value of the parameter ϕ, which is related to the ratios of characteristic times

$$\phi = \frac{E'^{11}\mu'^3C'^4Q_0}{K'^{14}} = \left(\frac{t_{mk}}{t_{m\tilde{m}}}\right)^{14/9} \quad (14)$$

(Examples of such trajectories are depicted in Fig. 2.)

In view of the dependence of the parameters $\mathscr{M}$, $\mathscr{K}$, $\mathscr{C}$, and $\mathscr{S}$ on time, see (13), it becomes apparent that the M-vertex corresponds to the origin of time, while the $\tilde{K}$-vertex corresponds to the end of time (except for an impermeable rock). Thus, given all the problem parameters, which completely define the number ϕ ($0 \leqslant \phi \leqslant \infty$), the system evolves with time (say time τ_{mk}) along a ϕ-trajectory, starting from the M-vertex (viscosity-storage-dominated regime: $\mathscr{K}_m = 0$, $\mathscr{C}_m = 0$) and ending at the $\tilde{K}$-vertex (toughness-leak-off dominated regime: $\mathscr{M}_{\tilde{k}} = 0$, $\mathscr{S}_{\tilde{k}} = 0$). For small values of ϕ (i.e., for small values of the ratio $t_{mk}/t_{m\tilde{m}}$), the trajectory is attracted by the K-vertex, and conversely for large values of ϕ the trajectory is attracted by the $\tilde{M}$-vertex.

The evolution of the fracture in the phase diagram $MK\tilde{K}\tilde{M}$ is, in part, linked to the multi-scale nature of the tip asymptotes [48], in particular to the transition from the viscosity edge $M\tilde{M}$ to the toughness edge $K\tilde{K}$ [29]. For example, along the viscosity edge, the tip aperture progressively changes from $w \sim s^{2/3}$ at the M-vertex to $w \sim s^{5/8}$ at the $\tilde{M}$-vertex [28].

2.3.2. Time scaling for viscosity-dominated regimes of propagation

Although the propagation of a hydraulic fracture generally depends on multiple time scales, in this paper we will restrict our discussion to particular cases where only one time scale is active. For the sake of brevity, we will only consider the transition between storage and leak-off dominated regimes along the $M\tilde{M}$ viscosity edge for which the time scale is $t_{m\tilde{m}}$, and the transition between viscosity and toughness-dominated regimes along the MK storage edge for which the time scale is t_{mk}. Each transition requires a separate scaling. In this Section, we provide the details of the scaling used to analyze the evolution of the fracture

along the $M\widetilde{M}$-edge, and in Appendix D we summarize the corresponding scaling for the MK-edge.

We introduce a length scale L_*, a time scale T_*, a characteristic fracture aperture W_*, and a characteristic (net) pressure P_* (all yet to be defined). The physical quantities of the problem are thus formally expressed as

$$x = L_*\chi, \quad y = L_*\zeta, \quad t = T_*\tau, \quad w = W_*\Omega,$$
$$p_f = P_*\Pi_f. \tag{15}$$

Furthermore, in order to scale the equations, we introduce the characteristic injection rate Q_0 and the characteristic stress σ_0 such that

$$Q = Q_0\psi(\tau), \quad \sigma = \sigma_0\varphi(\chi, \zeta), \tag{16}$$

where $\psi(\tau)$ and $\varphi(\chi, \zeta)$ are known functions, which we have already chosen to express in terms of the dimensionless time τ and space variables χ and ζ.

By introducing the above relations in the governing equations, it can readily be shown that four dimensionless groups emerge

$$\mathscr{G}_c = \frac{C'L_*^2}{Q_0 T_*^{1/2}}, \quad \mathscr{G}_e = \frac{L_*P_*}{E'W_*}, \quad \mathscr{G}_k = \frac{K'L_*^{1/2}}{E'W_*},$$
$$\mathscr{G}_m = \frac{\mu'Q_0}{P_*W_*^3}, \quad \mathscr{G}_v = \frac{Q_0 T_*}{L_*^2 W_*}. \tag{17}$$

Then, setting $\mathscr{G}_e = \mathscr{G}_c = \mathscr{G}_m = \mathscr{G}_v = 1$ yields four conditions to identify L_*, T_*, P_*, and W_*

$$L_* = \left(\frac{Q_0^5\mu'}{C'^8 E'}\right)^{1/7}, \quad T_* = \left(\frac{Q_0^6\mu'^4}{C'^{18}E'^4}\right)^{1/7},$$
$$W_* = \left(\frac{Q_0^3\mu'^2}{C'^2 E'^2}\right)^{1/7}, \quad P_* = \left(\frac{C'^6 E'^6\mu'}{Q_0^2}\right)^{1/7}. \tag{18}$$

On the one hand, the condition $\mathscr{G}_e = 1$ simply means that the average aperture scaled by the fracture dimension is of the same order as the average net pressure scaled by the elastic modulus, in accordance to elementary elasticity considerations. On the other hand, the conditions $\mathscr{G}_m = \mathscr{G}_c = 1$ (with $\mathscr{G}_m$ and $\mathscr{G}_c$ having the meaning of a dimensionless viscosity and leak-off coefficient, respectively) imply that T_* reflects the time of transition between a storage and a leak–off-dominated regime. Finally, the condition $\mathscr{G}_v = 1$ guarantees that the length scale L_* represents the characteristic dimension of the fracture at $t = T_*$. Finally, the dimensionless group $\mathscr{G}_k$ is renamed $\mathscr{K}$ in view of its meaning as the dimensionless toughness. The explicit expression for $\mathscr{K}$, in view of (18), is given by

$$\mathscr{K} = K'\left(\frac{1}{C'^2 E'^{11}Q_0\mu'^3}\right)^{1/14}. \tag{19}$$

However, when $C' > 0$, we will restrict our consideration to the $M\widetilde{M}$-edge for which $\mathscr{K} = 0$, with the implication that the tip aperture is no longer dominated by the LEFM singularity. Note that since the toughness K' does not appear in the characteristic quantities L_*, T_*, P_*, and W_*, there is

no degeneracy of the scaled solution in the limit $K' = 0$ in this particular scaling, which is referred to as the viscosity scaling. (The storage scaling, summarized in Appendix D, does not depend on the leak-off parameter C', and can therefore be used to investigate the limiting case of impermeable rocks, $C' = 0$.)

Finally, in the numerical scaling the governing equations transform to the following:

$$\Pi_f - \Sigma_0\varphi(\chi, \zeta) = -\frac{1}{8\pi}\int_{\mathscr{A}(\tau)}\frac{\Omega(\chi', \zeta', \tau)\mathrm{d}\mathscr{A}(\chi', \zeta')}{[(\chi' - \chi)^2 + (\zeta' - \zeta)^2]^{3/2}}, \tag{20}$$

$$\frac{\partial\Omega}{\partial\tau} + \frac{1}{\sqrt{(1 - \theta)\tau}} = \nabla\cdot(\Omega^3\nabla\Pi_f) + \psi(\tau)\delta(\chi, \zeta), \tag{21}$$

$$\lim_{\xi\to 0}\frac{\Omega}{\xi^{1/2}} = \mathscr{K}, \quad \lim_{\xi\to 0}\Omega^3\frac{\partial\Pi_f}{\partial\xi} = 0, \tag{22}$$

where Σ_0 is the scaled far-field stress σ_0/P_* and $\theta(\chi, \zeta)$ is defined as the dimensionless exposure time t_0/t. Note that it is advantageous to introduce the net pressure $\Pi = \Pi_f - \Sigma_0$, if $\varphi(\chi, \zeta) = 1$, i.e. if the far-field stress is homogeneous. The characteristic dimension of the fracture (e.g., the fracture radius) is $\gamma(\tau) = L/L_*$.

It is also convenient to introduce a scaling factor Q_* for the flow rate q, i.e.

$$q = Q_*\Psi. \tag{23}$$

By choosing

$$Q_* = \frac{W_*^3 P_*}{\mu'L_*} = \frac{Q_0}{L_*} = \left(\frac{C'^8 E'Q_0^2}{\mu'}\right)^{1/7}, \tag{24}$$

the scaled Poiseuille law can be written as

$$\Psi = -\Omega^3\nabla\Pi_f. \tag{25}$$

Finally, we note that the tip velocity $V(t)$, the critical quantity that legislates the asymptotic behavior of the solution, is naturally scaled along the $M\widetilde{M}$-edge by V_*

$$V_* = \frac{Q_*}{W_*} = \left(\frac{C'^{10}E'^3}{Q_0\mu'^3}\right)^{1/7}. \tag{26}$$

As shown in the next section, the asymptotic solutions for Ω and Π_f depend only on the scaled distance ξ from the fracture front $\mathscr{C}(t)$, and on the scaled tip velocity $v = V/V_*$.

3. Tip asymptotic behavior

It can be shown (see Appendix B) that the equations governing the aperture $w(s, t)$ and the net pressure $p(s)$ in the vicinity of the fracture front reduce to

$$\hat{q} = \frac{\hat{w}^3}{\mu'}\frac{\mathrm{d}\hat{p}}{\mathrm{d}s}, \quad \hat{q} = V\hat{w} + 2C'V^{1/2}s^{1/2},$$
$$\hat{p} = \frac{E'}{4\pi}\int_0^\infty\frac{\mathrm{d}\hat{w}}{\mathrm{d}z}\frac{\mathrm{d}z}{s - z}, \quad \lim_{s\to 0}\frac{\hat{w}}{s^{1/2}} = \frac{K'}{E'}, \tag{27}$$

where the propagation velocity V is given by the instantaneous local propagation velocity of the fracture front (Fig. 3). Note that the spatial variation of the far-field
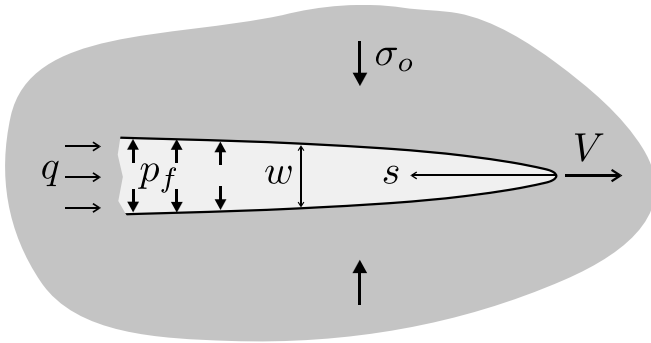
Fig. 3. Tip of an advancing fracture.

Fig. 4. Stationary solution $\widehat{\Omega}(\hat{\xi})$ for a semi-infinite hydraulic fracture propagating in the viscosity regime ($m\tilde{m}$ solution). The first terms of the asymptotic expansions of the solution in the near-field and the far-field are shown by dashed lines.

stress can be ignored when viewed at the tip scale, unless the stress field is discontinuous (in which case, the tip solution outlined here is not relevant). Eq. (27) are in fact identical to the governing equations for the problem of a semi-infinite fluid-driven fracture steadily propagating at a constant velocity and characterized by zero lag [24,26]. In other words, the tip asymptotic solution is given at any time by the solution of the stationary semi-infinite crack problem with a constant tip velocity corresponding to the current propagation speed of the finite fracture. The tip solution is thus autonomous.

3.1. Tip asymptotics along the leak-off-viscosity edge

The tip opening and net pressure asymptotics can advantageously be expressed as $\widehat{\Omega}(\hat{\xi})$ and $\widehat{\Pi}(\hat{\xi})$ where $\hat{\xi}$ is a normalized distance from the tip. These new tip-scaled quantities are defined as

$$s = \widehat{L}_* \hat{\xi}, \quad \hat{w} = \widehat{W}_* \widehat{\Omega}, \quad \hat{p} = \hat{p}_* \widehat{\Pi}, \tag{28}$$

where the tip length scale $\widehat{L}_*$, the characteristic tip opening $\widehat{W}_*$, and the characteristic pressure $\widehat{P}_*$ are given by

$$\widehat{L}_* = \frac{64 C'^6 E'^2}{V^5 \mu'^2}, \quad \widehat{W}_* = \frac{16 C'^4 E'}{V^3 \mu'}, \quad \widehat{P}_* = \frac{V^2 \mu'}{4 C'^2}. \tag{29}$$

Through the tip scaling, the dependence of the asymptotic solution upon the material parameters μ', E', C', as well as on the tip velocity V is entirely captured in the scaling factors $\widehat{L}_*$, $\widehat{W}_*$, and $\widehat{P}_*$. In other words, the tip asymptotic solution has a universal form $\widehat{\Omega}(\hat{\xi})$ and $\widehat{\Pi}(\hat{\xi})$. Although the complete tip solution has to be computed numerically, its series expansions for small and large $\hat{\xi}$ can be determined explicitly [48]. In particular, the series expansion for $\widehat{\Omega}(\hat{\xi})$ is given by

$$\hat{\xi} \to 0: \quad \widehat{\Omega} = \beta_{\tilde{m}0} \hat{\xi}^{5/8} + \beta_{\tilde{m}1} \hat{\xi}^{3/4} + \mathrm{O}(\hat{\xi}^{7/8}), \tag{30}$$

$$\hat{\xi} \to \infty: \quad \widehat{\Omega} = \beta_{m0} \hat{\xi}^{2/3} + \beta_{m1} \hat{\xi}^{1/2} + \mathrm{O}(\hat{\xi}^{1/3}) \tag{31}$$

where $\beta_{\tilde{m}0} \simeq 2.5336$, $\beta_{\tilde{m}1} \simeq 1.3016$, $\beta_{m0} = 2^{1/3} 3^{5/6}$, $\beta_{m1} = 1/2$. The complete semi-infinite tip solution is plotted in Fig. 4. Within a 5% accuracy, the viscosity-leak-off asymp-
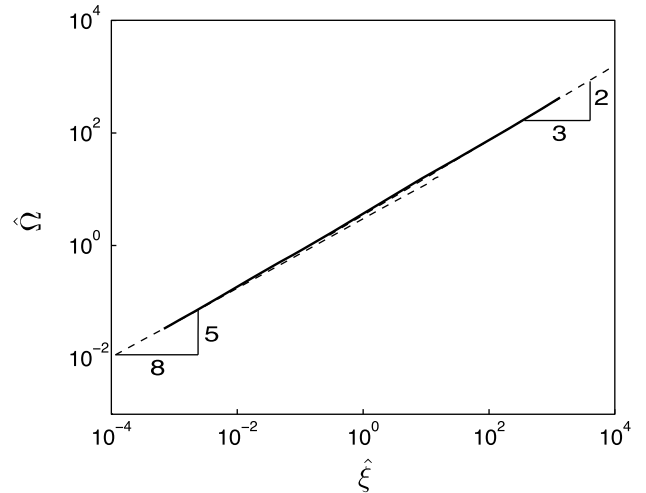
tote ($\beta_{\tilde{m}0} \hat{\xi}^{5/8}$) applies for $\hat{\xi} \lesssim \hat{\xi}_{\tilde{m}} \simeq 10^{-8}$ while the viscosity-storage asymptote ($\beta_{m0} \hat{\xi}^{2/3}$) applies for $\hat{\xi} \gtrsim \hat{\xi}_m \simeq 10^7$.

From the relationship between the two scalings, the tip asymptote can readily be expressed in terms of $\Omega(\xi)$

$$\widehat{\Omega} = \frac{W_*}{\widehat{W}_*} \Omega, \quad \hat{\xi} = \frac{L_*}{\widehat{L}_*} \xi, \tag{32}$$

which can be simplified as

$$\widehat{\Omega} = \frac{v^3}{16} \Omega, \quad \hat{\xi} = \frac{v^5}{64} \xi. \tag{33}$$

Thus the aperture Ω behaves according to the viscosity-storage asymptote, $\Omega \sim \beta_{m0} v^{1/3} \xi^{2/3}$ if $\xi \gtrsim \xi_m = 64 \hat{\xi}_m / v^5$, but according to the viscosity-leak-off asymptote $\Omega \sim 2^{1/4} \beta_{\tilde{m}0} v^{1/8} \xi^{5/8}$ if $\xi \lesssim \xi_{\tilde{m}} = 64 \hat{\xi}_{\tilde{m}} / v^5$.

Now consider a fracture for which the scaled extent is $\gamma = L/L_*$ so that the size of the near-tip region is $\varepsilon\gamma$, where ε is a small number. Evidence from both plane strain and the radial fractures suggest that this asymptotic umbrella extends to $\varepsilon = \mathrm{O}(10^{-1})$. In light of the above analysis, the relevance of either limiting asymptotic behavior, as far as the global solution is concerned, depends on the comparison of the length ξ_m or $\xi_{\tilde{m}}$ with $\varepsilon\gamma$. Hence, the tip will be locally dominated by the viscosity asymptote if $\varepsilon\gamma \gtrsim \xi_m$, but by the leak-off asymptote if $\varepsilon\gamma \lesssim \xi_{\tilde{m}}$.

As discussed in Sections 4 and 5, our reference length for the application of the tip asymptote will be the characteristic dimension Δs of a grid element and the asymptote will be imposed in a weak form – via the volume. The above considerations show that the nature of the tip asymptote to be imposed in a tip element depends critically on the local tip velocity. Indeed, the aperture of the tip element is dominated by the viscosity asymptote if the tip velocity $v \gtrsim (64 \hat{\xi}_m / \Delta s)^{1/5}$, but by the viscosity leak-off asymptote if $v \lesssim (64 \hat{\xi}_{\tilde{m}} / \Delta s)^{1/5}$.
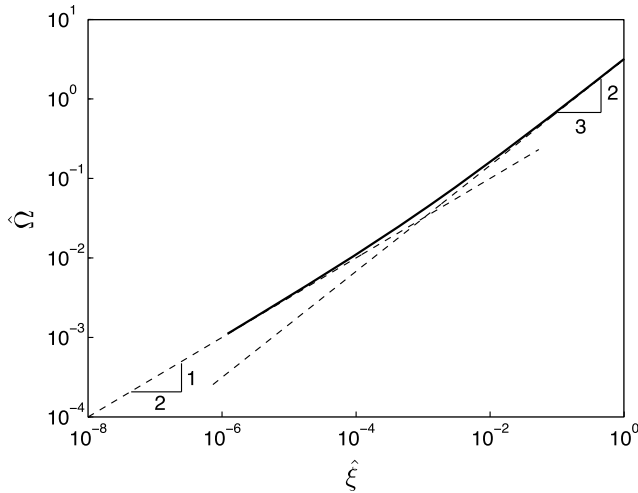
Fig. 5. Stationary solution $\widehat{\Omega}(\hat{\xi})$ for a semi-infinite hydraulic fracture propagating in the storage regime (*mk* solution). The first terms of the asymptotic expansions of the solution in the near-field and the far-field are shown by dashed lines.

3.1.1. Tip asymptotics along the viscosity-toughness edge

The corresponding tip asymptotic behavior along the storage edge of phase space is summarized in Appendix D. In this case the series expansion for $\widehat{\Omega}(\hat{\xi})$ is given by

$$\hat{\xi} \to 0: \quad \widehat{\Omega} = \hat{\xi}^{1/2} + 4\pi\hat{\xi} + \frac{128}{3}\hat{\xi}^{3/2}\ln\hat{\xi} + O(\hat{\xi}^{3/2}), \quad (34)$$

$$\hat{\xi} \to \infty: \quad \widehat{\Omega} = \beta_0\hat{\xi}^{2/3} + \beta_1\hat{\xi}^h + O(\hat{\xi}^h), \quad (35)$$

where $\beta_0 = \beta_{m0} = 2^{1/3} \cdot 3^{5/6}$, $\beta_1 \simeq 0.0371887$, and $h \simeq 0.138673$. The complete semi-infinite tip solution is plotted in Fig. 5 where it can be seen that the LEFM behavior ($\hat{\xi}^{1/2}$) applies for $\hat{\xi} \lesssim \hat{\xi}_k \simeq 10^{-5}$ and the viscous dissipation asymptote ($\beta_0\hat{\xi}^{2/3}$) for $\hat{\xi} \gtrsim \hat{\xi}_m \simeq 10^{-1}$.

4. Discrete equations

4.1. Preamble

In this section we describe the discretization of the equations governing the propagation of a hydraulic fracture on a rectangular Eulerian mesh. While the numerical schemes used to approximate the elasticity and lubrication equations are rather classical, the discrete equations for the elements containing the fracture front require special attention, as they have to account for the tip asymptotic behavior. The detailed presentation of the algorithm devised to evolve the front is left to Section 5, and in this section we deal with the formulation of the discrete equations that have to be solved for the opening and pressures at the centers of the grid elements, assuming that the front position has already been established.

A fixed uniform rectangular mesh with spacings $\Delta\chi$ and $\Delta\zeta$ in the two coordinate directions is first selected so as to

encompass the region into which the fracture will grow. The fracture surface $\mathscr{A}$ is therefore covered by rectangular elements $\Delta\mathscr{A}_{m,n}$ such that $\mathscr{A} \subset \bigcup_{m,n}\Delta\mathscr{A}_{m,n}$. (The element $\Delta\mathscr{A}_{m,n}$ is indexed on a two-dimensional lattice.) Furthermore, it is notionally profitable to decompose the fracture footprint into two regions, the "channel region" $\mathscr{A}^c$ comprising the elements that are completely filled with fluid and the "tip region" $\mathscr{A}^t$ consisting of those elements that are partially filled. The elements within $\mathscr{A}^c$ that are on the boundary with $\mathscr{A}^t$ (i.e., those elements of $\mathscr{A}^c$ that have at least one north, south, east or west neighbor that is in $\mathscr{A}^t$) form the ribbon of elements, which we denote by the set $\partial\mathscr{A}^c$, on which the boundary values for the solution to the Eikonal equation are defined. This solution is then used to identify the location of the fracture front.

Given the actual (or trial) fracture front at time t and the evolution of this front since the onset of injection, determining the aperture and pressure fields relies on the simultaneous solution of the elasticity Eq. (20) and the lubrication Eq. (21), while taking into account the appropriate tip asymptotic behavior and the amount of fluid injected into the fracture. The numerical solution of this system of equations involves the displacement discontinuity (DD) method [43] for discretizing the elasticity equation, a finite volume scheme for approximating the lubrication equation, and a weak formulation of the tip asymptotics that is implemented by computing both the volume of fluid stored in a tip element in accordance with the asymptotic field and the amount of fluid that has leaked-off from a tip element.

This discretization process yields an extremely stiff system of non-linear equations for the current fracture widths in the channel elements and the pressures at the tip element centers. We describe a fixed-point iterative scheme to compute the mixed field variables comprising the channel width increments and the tip pressures.

4.2. Discretized elasticity equation

The elasticity Eq. (20) is discretized by assuming that the fracture opening $\Omega(\chi, \zeta, \tau)$ is piecewise constant over each rectangular element $\Delta\mathscr{A}_{m,n}$, i.e.

$$\Omega(\chi, \zeta, \tau) = \sum_{m,n} \Omega_{m,n}(\tau)H_{m,n}(\chi, \zeta), \quad (36)$$

in which

$$H_{m,n}(\chi, \zeta) = \begin{cases} 1 & \text{for } (\chi, \zeta) \in \Delta\mathscr{A}_{m,n}, \\ 0 & \text{for } (\chi, \zeta) \notin \Delta\mathscr{A}_{m,n} \end{cases} \quad (37)$$

is the characteristic function for element (m, n). Substituting this expansion into the integral Eq. (20) and evaluating the pressures at the collocation points located at the element centers, yields a system of algebraic equations of the form

$$\Pi_{k,l}(\tau) = \sum_{m,n} C_{k-m,l-n}\Omega_{m,n}(\tau), \quad (38)$$

where

$$C_{k-m,l-n} = -\frac{1}{8\pi} \left[\frac{\sqrt{(\chi_k - \chi)^2 + (\zeta_l - \zeta)^2}}{(\chi_k - \chi)(\zeta_l - \zeta)} \right]_{\chi=\chi_m-\Delta\chi/2, \zeta=\zeta_n-\Delta\zeta/2}^{\chi=\chi_m+\Delta\chi/2, \zeta=\zeta_n+\Delta\zeta/2}.$$

It is also convenient to express the discretized elasticity Eq. (38) in the following operator form

$$\mathbf{\Pi} = \mathbf{C}\mathbf{\Omega}. \tag{39}$$

4.3. Discretized Reynolds equation

In order to smooth the singular leak-off term in (21) we integrate with respect to τ over the time interval $[\tau - \Delta\tau, \tau]$ to obtain the following integral form

$$\Omega(\chi, \zeta, \tau')|_{\tau-\Delta\tau}^{\tau} + 2\left(\sqrt{\tau - \tau_0} - \sqrt{\tau - \Delta\tau - \tau_0}\right)$$
$$= \int_{\tau-\Delta\tau}^{\tau} \mathbf{\nabla} \cdot \left(\Omega^3 \mathbf{\nabla}\Pi_{\mathrm{f}}\right) \mathrm{d}\tau' + \delta(\chi, \zeta) \int_{\tau-\Delta\tau}^{\tau} \psi(\tau')\mathrm{d}\tau'. \tag{40}$$

Consistent with the backward Euler scheme, we approximate the first integral on the right side of (40) by the right-hand rule and integrate over an element $\Delta\mathscr{A}_{i,j}$ to obtain the following approximation

$$\int_{\Delta\mathscr{A}_{i,j}} \Omega(\tau) - \Omega(\tau - \Delta\tau)\mathrm{d}\mathscr{A}$$
$$= \Delta\tau \left[\int_{\Delta\mathscr{C}_{i,j}} \Omega^3 \frac{\partial\Pi}{\partial n}\mathrm{d}\mathscr{C} \right]_{\tau} - 2\int_{\Delta\mathscr{A}_{i,j}} \left(\sqrt{\tau - \tau_0(\chi, \zeta)}\right.$$
$$\left. -\sqrt{\tau - \Delta\tau - \tau_0(\chi, \zeta)}\right)\mathrm{d}\mathscr{A} + \delta_{i,0}\delta_{j,0}\int_{\tau-\Delta\tau}^{\tau} \psi(\tau')\mathrm{d}\tau', \tag{41}$$

where $\delta_{i,j}$ is the Kronecker delta symbol. In the above, we have assumed that the injection point is located at the center of element $\Delta\mathscr{A}_{0,0}$. In order to discretize the integral form of the fluid flow Eq. (41) in a way that is compatible with (38) we use the pressures $\Pi_{k,l}(\tau)$ and average widths $\Omega_{k,l}(\tau)$ sampled at element centers along with central difference approximations to the pressure gradients on the boundaries of the elements, and divide by $\Delta\chi\Delta\zeta$ to obtain

$$\Omega_{i,j}(\tau) - \Omega_{i,j}(\tau - \Delta\tau) = \Delta\tau[A(\Omega)\Pi]_{i,j} - \frac{\Delta\mathscr{L}_{i,j}}{\Delta\chi\Delta\zeta}$$
$$+ \frac{\delta_{i,0}\delta_{j,0}}{\Delta\chi\Delta\zeta}\int_{\tau-\Delta\tau}^{\tau}\psi(\tau')\mathrm{d}\tau', \tag{42}$$

where $A(\Omega)$ is the difference operator defined by

$$[A(\Omega)\Pi]_{k,l} = \frac{1}{\Delta\chi}\left(\Omega_{k+\frac{1}{2},l}^3\frac{(\Pi_{k+1,l} - \Pi_{k,l})}{\Delta\chi} - \Omega_{k-\frac{1}{2},l}^3\frac{(\Pi_{k,l} - \Pi_{k-1,l})}{\Delta\chi}\right)$$
$$+ \frac{1}{\Delta\zeta}\left(\Omega_{k,l+\frac{1}{2}}^3\frac{(\Pi_{k,l+1} - \Pi_{k,l})}{\Delta\zeta} - \Omega_{k,l-\frac{1}{2}}^3\frac{(\Pi_{k,l} - \Pi_{k,l-1})}{\Delta\zeta}\right) \tag{43}$$

and $\Delta\mathscr{L}_{i,j}$ represents the volume of fluid that leaks from the element (i,j) over the time-step $\Delta\tau$ and is defined by

$$\Delta\mathscr{L}_{i,j} = 2\int_{\Delta\mathscr{A}_{i,j}} \left(\sqrt{\tau - \tau_0(\chi, \zeta)} - \sqrt{\tau - \Delta\tau - \tau_0(\chi, \zeta)}\right)\mathrm{d}\mathscr{A}. \tag{44}$$

Zero flux boundary conditions are implemented in tip elements by removing those terms associated with the element faces having zero boundary fluxes from the difference operator.

Various approximations to (44) are possible. For example, a midpoint rule approximation along with the definition of the appropriate elemental trigger time $\tau_{k,l}$, which is an average time of first exposure for element (k, l), is relatively accurate for internal elements. For tip elements, in which the integrand in (44) varies more rapidly, a more precise approximation is discussed in the next subsection. Since the allocation of the elemental trigger time should occur at the moment that a tip element fills and therefore transitions to the channel elements, we also discuss the capture of trigger times in the next subsection dealing with tip elements.

It is convenient to express the discrete lubrication Eq. (42) in the following operator form

$$\Delta\mathbf{\Omega} = \Delta\tau A(\mathbf{\Omega})\mathbf{\Pi} + \Delta\tau\mathbf{\Gamma}, \tag{45}$$

where $A(\mathbf{\Omega})$ is the second order difference operator defined on the right side of (43) and $\mathbf{\Gamma}$ represents the vector of sink and source terms.

4.4. Calculation of fluid volumes in tip elements

4.4.1. Tip quantities and notation

Fig. 6 illustrates a partially fluid-filled tip element with the front labelled as MN. The flow domain $\Delta\mathscr{A}_\ell$ is the region shown shaded in gray, which is bounded by the closed contour $\Delta\mathscr{C}_\ell = \text{ABMNDA}$. The front segment MN is orthogonal to the front velocity vector $\mathbf{v}$, which is inclined by an angle α to the χ-axis. Let $\Delta\mathscr{C}_\ell^*$ denote the open contour NDABM (i.e. $\Delta\mathscr{C}_\ell$ minus the front segment MN). Next consider the orthogonal system of axes $(\bar{\xi}, \bar{\eta})$ with the $\bar{\xi}$-axis parallel to $\mathbf{v}$ and with its origin at the point of first entry of the front into the element (corner A for the

Fig. 6. Tip element.

case sketched in Fig. 6). The abscissa of the front in the $(\bar{\bar{\xi}}, \bar{\eta})$ coordinates is given by $\bar{\bar{\xi}} = \ell$ and thus $\xi = \ell - \bar{\bar{\xi}}$. We will refer to ℓ simply as the (relative) front position in the tip element.

Evidently, given the element side lengths $\Delta\chi$ and $\Delta\zeta$, the geometry of the flow domain $\Delta\mathscr{A}_\ell$ is completely defined by α and ℓ. By simple projection, it can be shown that ℓ takes the maximum value λ given by

$$\lambda = \Delta\chi \cos\alpha + \Delta\zeta \sin\alpha. \tag{46}$$

Thus the front is in the element if $0 < \ell < \lambda$, and the element is partially filled with fluid. We also introduce the areal filling fraction $\mathscr{F}(\ell)$ $(0 < \mathscr{F} < 1)$ defined as

$$\breve{F}(\ell) = \begin{cases} mF(\ell), & 0 \leqslant \ell \leqslant \xi_0, \ m \neq \infty, \\ m[F(\ell) - F(\ell - \xi_0)], & \xi_0 \leqslant \ell \leqslant \lambda - \xi_0, \ m \neq \infty, \\ m[F(\ell) - F(\ell - \xi_0) - F(\ell + \xi_0 - \lambda)], & \lambda - \xi_0 \leqslant \ell \leqslant \lambda, \ m \neq \infty, \\ m[F(\ell) - F(\ell - \xi_0) - F(\ell + \xi_0 - \lambda) + F(\ell - \lambda)] & \lambda < \ell, \ m \neq \infty \\ \Delta\eta f(\ell), & 0 \leqslant \ell \leqslant \Delta\xi, \ m = \infty, \\ \Delta\eta[f(\ell) - f(\ell - \Delta\xi)] & \Delta\xi < \ell, \ m = \infty \end{cases} \tag{54}$$

$$\mathscr{F} = \frac{\Delta\mathscr{A}_\ell}{\Delta\chi\Delta\zeta}. \tag{47}$$

The shape/geometry of the flow domain also depends on the factor m defined as

$$m = \frac{1}{\cos\alpha\sin\alpha} \tag{48}$$

and on the length ξ_0 given by

$$\xi_0 = \begin{cases} \Delta\zeta\sin\alpha, & 0 < \tan\alpha \leqslant \frac{\Delta\chi}{\Delta\zeta}, \\ \Delta\chi\cos\alpha, & \frac{\Delta\chi}{\Delta\zeta} \leqslant \tan\alpha < \infty. \end{cases} \tag{49}$$

Indeed, four different flow configurations arise depending on ℓ, λ, ξ_0, and m. If $m = \infty$, the front is parallel to one of the fixed coordinate axes (χ or ζ) and $\Delta\mathscr{A}_\ell$ is a rectangle. If $m \neq \infty$, $\Delta\mathscr{A}_\ell$ is either a triangle, quadrilateral, or a pentagon depending on wether $0 < \ell < \xi_0$, or $\xi_0 < \ell < \lambda - \xi_0$, or $\lambda - \xi_0 < \ell < \lambda$, respectively.

Finally, it is convenient to define the power law function $\Xi_\alpha(\xi)$ as

$$\Xi_\alpha = \xi^\alpha, \quad \alpha > -1. \tag{50}$$

4.4.2. Integral over the flow domain

Formulation of the discrete equations that are required to allocate fluid volume within a tip element relies on the evaluation of surface integrals of the form

$$I = \int_{\Delta\mathscr{A}_\ell} \frac{\mathrm{d}f}{\mathrm{d}\xi} \mathrm{d}\mathscr{A} = \int_{\Delta\mathscr{A}_\ell} \mathbf{V}_{(\xi,\eta)} \cdot (f, 0) \mathrm{d}\mathscr{A}, \tag{51}$$

where the function $f(\xi)$ vanishes at $\xi = 0$. Using the divergence theorem, we can rewrite (51) as

$$I = \int_{\Delta\mathscr{C}_\ell} (f, 0) \cdot (n_\xi, n_\eta) \mathrm{d}\mathscr{C} = -\int_{\Delta\mathscr{C}_\ell} f n_{\bar{\xi}} \mathrm{d}\mathscr{C}, \tag{52}$$

where $n_{\bar{\xi}}$ is the component of the external unit normal to the contour $\Delta\mathscr{C}_\ell$ projected onto the $\bar{\xi}$-axis. The integration contour can also be reduced from $\Delta\mathscr{C}_\ell$ to $\Delta\mathscr{C}_\ell^*$, since $f(0) = 0$. It is shown in Appendix A, that the integral $I(\ell)$ can be expressed as

$$I = \breve{F}(\ell), \tag{53}$$

where $\breve{F}(\ell)$ is defined as

and $F(\xi)$ is defined as

$$F(\xi) = \int_0^\xi f(u) \mathrm{d}u. \tag{55}$$

It should be noted that the special case $\lambda < \ell$ for interior elements, in which the interval of integration is $0 \leqslant \xi \leqslant \lambda$ (see the definition of $J(\ell)$ in Appendix A), has been included in the definition of the operator $\breve{F}(\ell)$. The lengths $(\Delta\xi, \Delta\eta)$ that enter in the expressions of $\breve{F}(\ell)$ for $m = \infty$ are equal to $(\Delta\zeta, \Delta\chi)$ if $\alpha = \pm\pi/2$ and to $(\Delta\chi, \Delta\zeta)$ if $\alpha = 0, \pi$.

As a simple application of these formulae, the surface filling fraction $\mathscr{F}(\ell)$ defined in (47) can, using the notation (50) for the power law function, be conveniently expressed as

$$\mathscr{F} = \frac{1}{\Delta\chi\Delta\zeta} \int_{\Delta\mathscr{A}_\ell} \frac{\mathrm{d}\Xi_1}{\mathrm{d}\xi} \mathrm{d}\mathscr{A}. \tag{56}$$

Hence, $\mathscr{F}(\ell)$ can simply be computed as

$$\mathscr{F} = \frac{\breve{\Xi}_2(\ell)}{2\Delta\chi\Delta\zeta}. \tag{57}$$

4.4.3. Leak-off volume in tip elements and trigger times

The leak-off volume $\Delta\mathscr{L}_{i,j}$ for a tip element is calculated as follows. Defining τ_e to be the time that the front first enters the element, replacing τ and τ_0 in the integral for $\Delta\mathscr{L}_{ij}$ by $\tau = \tau_e + \ell/v$ and $\tau_0 = \tau_e + \xi/v$ respectively, and applying (53) we obtain the following expression for $\Delta\mathscr{L}_{i,j}$ for tip elements

$$\Delta\mathscr{L}_{i,j} = 2v^{-1/2}\int_{\Delta\mathscr{A}_{i,j}}\left[\frac{\mathrm{d}}{\mathrm{d}\xi}\left(\frac{2}{3}\Xi_{\frac{3}{2}}\right)\right]_{\tau-\Delta\tau}^{\tau}\mathrm{d}\mathscr{A}$$
$$= \frac{8}{15}v^{-1/2}\left[\breve{\Xi}_{\frac{5}{2}}(\ell_\tau) - \breve{\Xi}_{\frac{5}{2}}(\ell_{\tau-\Delta\tau})\right]. \tag{58}$$

Following a similar procedure for interior elements in which v is the velocity with which the front was moving when it traversed element e, we obtain the same formula as in (58), but in which ℓ_τ is the total distance the front would have moved at the velocity v since the fluid front first entered the element, i.e. $\ell_\tau = v(\tau - \tau_e) > \lambda$ and $\ell_{\tau-\Delta\tau}$ is the total distance the retarded front would have moved since τ_e, i.e. $\ell_{\tau-\Delta\tau} = v(\tau - \Delta\tau - \tau_e)$. This represents a more accurate, but also more complex, alternative to the midpoint approximation for interior elements discussed above.

We are now able to compute the leak-off trigger time $\tau_{i,j}$ for channel element (i,j) which is required for the calculation of the source-sink term $\Gamma_{i,j}$ in (45). Let τ_x denote the time at which the front leaves an element (i.e. the instant the element transitions from the tip to the channel region) which is given by $\tau_x = \tau - (\ell_\tau - \lambda)/v$. In order to implement a midpoint approximation to the integrals in (44) we need to estimate the time the fracture front reaches the midpoint of an element, which is given by

$$\tau_{i,j} = \frac{1}{2}(\tau_e + \tau_x). \tag{59}$$

4.4.4. Volume of tip elements
The elemental volumes associated with the particular tip asymptotes considered here are as follows

- Near the K-vertex, $\Omega \sim \xi^{1/2}$

$$\Omega_{i,j}\Delta\chi\Delta\zeta = \int_{\Delta\mathscr{A}_\ell}\frac{\mathrm{d}}{\mathrm{d}\xi}\left(\frac{2}{3}\Xi_{\frac{3}{2}}\right)\mathrm{d}\mathscr{A} = \frac{4}{15}\breve{\Xi}_{\frac{5}{2}}(\ell).$$

- Near the M-vertex, $\Omega \sim \beta_{m0}v^{1/3}\xi^{2/3}$

$$\Omega_{i,j}\Delta\chi\Delta\zeta = \beta_{m0}v^{1/3}\int_{\Delta\mathscr{A}_\ell}\frac{\mathrm{d}}{\mathrm{d}\xi}\left(\frac{3}{5}\Xi_{\frac{5}{3}}\right)\mathrm{d}\mathscr{A} = \frac{9}{40}\beta_{m0}v^{1/3}\breve{\Xi}_{\frac{8}{3}}(\ell).$$

- Near the $\widetilde{M}$-vertex, $\Omega \sim 2^{1/4}\beta_{\tilde{m}0}v^{1/8}\xi^{5/8}$

$$\Omega_{i,j}\Delta\chi\Delta\zeta = 2^{1/4}\beta_{\tilde{m}0}v^{1/8}\int_{\Delta\mathscr{A}_\ell}\frac{\mathrm{d}}{\mathrm{d}\xi}\left(\frac{8}{13}\Xi_{\frac{13}{8}}\right)\mathrm{d}\mathscr{A}$$
$$= \frac{2^{25/4}}{273}\beta_{\tilde{m}0}v^{1/8}\breve{\Xi}_{\frac{21}{8}}(\ell).$$

Thus, once ℓ and $\overrightarrow{n}$ are determined using the level set algorithm discussed in Section 5 – see (79) and (80), both $\Omega_{i,j}(\tau)$ and $\Delta\mathscr{L}_{i,j}$ in (42) are known. All that remains to be determined is the pressure $\Pi_{i,j}$ within the tip elements, as elaborated next.

4.5. Solution of the mixed-variable coupled equations

Once the front position in a tip element is defined, the width profile within the element and the corresponding

tip fluid volume is determined by the applicable tip asymptotic solution as shown above. To conserve fluid volume, average width values calculated from the tip fluid volumes must then be allocated to the DD element tip width values in a way that is consistent with the volume of fluid that has flowed into the tip element minus the fluid volume lost due to leak-off. Thus the primary unknowns within the tip elements become the fluid pressures, which are calculated in such a way that mass balance is preserved. We now provide details of the computation of the mixed field variables.

Since we treat the tip and channel variables differently, we introduce a superscript c to represent a channel variable and a superscript t to represent a tip variable. Thus $\mathbf{\Omega}^c$ and $\mathbf{\Pi}^c$ represent the vectors containing the channel widths and fluid pressures respectively, while $\mathbf{\Omega}^t$ and $\mathbf{\Pi}^t$ represent the corresponding tip variables. From (39) the channel pressures can be expressed as

$$\mathbf{\Pi}^c = \mathbf{C}^{cc}\mathbf{\Omega}^c + \mathbf{C}^{ct}\mathbf{\Omega}^t, \tag{60}$$

where $\mathbf{C}^{cc}$ and $\mathbf{C}^{ct}$ represent the channel-to-channel and tip-to-channel Green's function influence matrices. From (45) the channel lubrication equation can be written in the form

$$\Delta\mathbf{\Omega}^c = \mathbf{\Omega}^c - \mathbf{\Omega}_0^c = \Delta\tau(\mathbf{A}^{cc}\mathbf{\Pi}^c + \mathbf{A}^{ct}\mathbf{\Pi}^t) + \Delta\tau\mathbf{\Gamma}^c, \tag{61}$$

where $\mathbf{\Omega}_0^c$ is the channel width at the previous time step. For the tip, the lubrication Eq. (45) can be re-written as

$$\Delta\mathbf{\Omega}^t = \mathbf{\Omega}^t - \mathbf{\Omega}_0^t = \Delta\tau(\mathbf{A}^{tc}\mathbf{\Pi}^c + \mathbf{A}^{tt}\mathbf{\Pi}^t) + \Delta\tau\mathbf{\Gamma}^t. \tag{62}$$

Now using (60) to eliminate $\mathbf{\Pi}^c$ from (61) and (62) and re-arranging terms we obtain the following system of non-linear equations for the channel width increments and tip pressures:

$$\begin{bmatrix} \mathbf{I} - \Delta\tau\mathbf{A}^{cc}\mathbf{C}^{cc} & -\Delta\tau\mathbf{A}^{ct} \\ -\Delta\tau\mathbf{A}^{tc}\mathbf{C}^{cc} & -\Delta\tau\mathbf{A}^{tt} \end{bmatrix}\begin{bmatrix} \Delta\mathbf{\Omega}^c \\ \mathbf{\Pi}^t \end{bmatrix}$$
$$= \begin{bmatrix} \Delta\tau\mathbf{A}^{cc}(\mathbf{C}^{cc}\mathbf{\Omega}_0^c + \mathbf{C}^{ct}\mathbf{\Omega}^t) + \Delta\tau\mathbf{\Gamma}^c \\ -\Delta\mathbf{\Omega}^t + \Delta\tau\mathbf{A}^{tc}(\mathbf{C}^{cc}\mathbf{\Omega}_0^c + \mathbf{C}^{ct}\mathbf{\Omega}^t) + \Delta\tau\mathbf{\Gamma}^t \end{bmatrix}. \tag{63}$$

Since the front positions and therefore the tip widths $\mathbf{\Omega}^t$ are known, the solution to this system of equations yields the channel widths $\mathbf{\Omega}^c = \mathbf{\Omega}_0^c + \Delta\mathbf{\Omega}^c$ and the tip pressures $\mathbf{\Pi}^t$. By freezing the matrix coefficients and right hand side components at the current trial solution, we obtain a linear system for $\Delta\mathbf{\Omega}^c$ and $\mathbf{\Pi}^t$. Efficient preconditioners for this system of linear Eq. (63) can be found in [33,49]. The value of $\Delta\mathbf{\Omega}^c$ is then used to update the trial solution $\mathbf{\Omega}^c$ and the fixed-point iteration is continued until convergence is achieved.

5. The implicit level set algorithm

In this section we present the implicit level set algorithm that is used to update the position of the front given the new estimate of the fracture width $\mathbf{\Omega}$ associated with the current footprint. The algorithm is based on the critical assumption that the elements on the boundary of the chan-

nel region $\partial\mathscr{A}^c$, i.e. those channel elements that have at least one tip element as a neighbor are still under the asymptotic umbrella.

5.1. Inverting the tip asymptotic relation

We first express the tip asymptotic relation in the general form

$$\Omega \sim \mathscr{W}(\xi; v). \tag{64}$$

For each of the elements on the boundary of the channel region $\partial\mathscr{A}^c$, we then invert the tip asymptotic relation to determine the required boundary values for the crossing-time map $\mathscr{T}(\chi, \zeta)$ as follows

$$\mathscr{T}(\chi, \zeta) = -\xi \sim -\mathscr{W}^{-1}(\Omega; v) \quad \text{for all } (\chi, \zeta) \in \partial\mathscr{A}^c. \tag{65}$$

We have assumed that $\mathscr{T}(\chi, \zeta) < 0$ for points that are located inside the front and that (65) is a local approximation to the signed distance function. We now illustrate this procedure in the following three special cases.

5.1.1. Toughness-storage regime
In this case the asymptotic relation (64) reduces to the form

$$\Omega \overset{\xi\to 0}{\sim} \xi^{\frac{1}{2}}, \tag{66}$$

which can easily be inverted to yield

$$\mathscr{T}(\chi, \zeta) = -\xi \sim -\Omega^2 \quad \text{for all } (\chi, \zeta) \in \partial\mathscr{A}^c. \tag{67}$$

We observe that in this particular case the front location does not involve the velocity field. This situation is similar to that of the dry crack [38,39], in which Paris' growth rule is invoked in order to arrive at a pseudo-velocity field that is required for the front evolution process via the classic level set algorithm. That the implicit level set algorithm that we propose does not require the velocity field is an asset for this problem.

5.1.2. Viscosity-storage regime
In this case the asymptotic relation (64) reduces to the form

$$\Omega \overset{\xi\to 0}{\sim} \beta_{m0} v^{1/3} \xi^{2/3}. \tag{68}$$

Inverting this asymptotic relation we obtain

$$\mathscr{T}(\chi, \zeta) = -\xi \sim -\left(\frac{\Omega}{\beta_{m0} v^{1/3}}\right)^{\frac{3}{2}} \quad \text{for all } (\chi, \zeta) \in \partial\mathscr{A}^c. \tag{69}$$

Comparing (67)–(69) we observe that the latter case involves the normal velocity v of the front. Determining the normal velocity from (10) is undesirable as it involves an indeterminate limit, so our approach is to determine the velocity as part of the inversion process. To this end let $\mathscr{T}_0(\chi, \zeta)$ represent the crossing-time map associated with the previous time $\tau - \Delta\tau$, which is already known. The local normal velocity of the front can then be expressed as

$$v = -\frac{\mathscr{T} - \mathscr{T}_0}{\Delta\tau}. \tag{70}$$

Eliminating v from (69) using (70) we obtain the following cubic equation for $\mathscr{T}(\chi, \zeta)$

$$\mathscr{T}^3 - \mathscr{T}_0 \mathscr{T}^2 + b = 0, \tag{71}$$

where $b = \Delta\tau(\frac{\Omega}{\beta_{m0}})^3 > 0$. Applying Descartes' sign rule we observe that (71) has at most one negative real root. If $d = b[b - 4(\frac{\mathscr{T}_0}{3})^3] > 0$ then there is one real root, which is given by

$$\mathscr{T} = \frac{\mathscr{T}_0}{3} - \left(\frac{c}{2} - \frac{\sqrt{d}}{2}\right)^{\frac{1}{3}} - \left(\frac{c}{2} + \frac{\sqrt{d}}{2}\right)^{\frac{1}{3}},$$

where $c = b - 2(\frac{\mathscr{T}_0}{3})^3$. If $d < 0$ there are three real roots and the desired negative root is given by

$$\mathscr{T} = \frac{\mathscr{T}_0}{3} - 2\left(\frac{|\mathscr{T}_0|}{3}\right) \sin\left(\frac{\theta}{3} + \frac{\pi}{6}\right)$$

$$\text{where } \theta = \tan^{-1}\left(\frac{\sqrt{-d}}{-c}\right), \quad 0 \leqslant \theta \leqslant \pi.$$

5.1.3. Viscosity-leak-off regime
In this case the asymptotic relation (64) reduces to the form

$$\Omega \overset{\xi\to 0}{\sim} 2^{1/4} \beta_{\tilde{m}0} v^{1/8} \xi^{5/8}. \tag{72}$$

Inverting this asymptotic relation yields

$$\mathscr{T}(\chi, \zeta) = -\xi \sim -\left(\frac{\Omega}{2^{1/4} \beta_{\tilde{m}0} v^{1/8}}\right)^{\frac{8}{5}} \quad \text{for all } (\chi, \zeta)$$

$$\in \partial\mathscr{A}^c. \tag{73}$$

Proceeding as in the viscosity-dominated regime we obtain

$$\mathscr{T}^6 - \mathscr{T}_0 \mathscr{T}^5 - b = 0, \tag{74}$$

where $b = \Delta\tau(\frac{\Omega}{2^{1/4}\beta_{\tilde{m}0}})^8 > 0$. Although (74) does not have a closed form solution, Descartes' sign rule implies that the polynomial has a maximum of one negative and one positive real root. Since the coefficients of (74) are real, so that the roots must be real or appear in complex conjugate pairs, there are either two real roots or no real roots at all. The condition for transition from two real roots to none occurs when the two real roots coalesce to form a single root at a turning point given by

$$6\mathscr{T}^5 - 5\mathscr{T}_0 \mathscr{T}^4 = \mathscr{T}^4(6\mathscr{T} - 5\mathscr{T}_0) = 0.$$

The two options are that $\mathscr{T} = 0$ which implies that $b = 0$, or $\mathscr{T} = \frac{5\mathscr{T}_0}{6}$, which, according to (74), implies that $b = -5^5(\frac{\mathscr{T}_0}{6})^6 < 0$ – both of which are impossible. Thus (74) has only one negative root that can be determined numerically.

5.2. Locating the front using the FMM

Having determined the correct boundary conditions $\mathcal{T}(\chi, \zeta)$ along the ribbon of channel elements $\partial\mathscr{A}^c$ that border on the tip region, we are now in a position to locate the free boundary by solving the Eikonal equation

$$|\nabla\mathcal{T}(\chi, \zeta)| = 1. \tag{75}$$

This is perhaps the simplest Hamilton–Jacobi equation which is often used in the level set literature to initialize the signed distance function. We note that the normal velocity function is not required here since any expressions involving the velocity field have been accounted for implicitly in the process of inverting the tip asymptotic expansion as described above.

There is an extensive literature, see for example [50,51], on the solution of (75). Thus, for the sake of brevity, we only outline the simplest first order scheme referring the reader to the above texts and references therein. We consider the following one-sided difference approximation to (75)

$$\left[\max\left(\frac{\mathcal{T}_{i,j} - \mathcal{T}_{i-1,j}}{\Delta\chi}, \frac{\mathcal{T}_{i,j} - \mathcal{T}_{i+1,j}}{\Delta\chi}, 0\right)\right]^2$$
$$+ \left[\max\left(\frac{\mathcal{T}_{i,j} - \mathcal{T}_{i,j-1}}{\Delta\zeta}, \frac{\mathcal{T}_{i,j} - \mathcal{T}_{i,j+1}}{\Delta\zeta}, 0\right)\right]^2 = 1. \tag{76}$$

By defining

$$\mathcal{T}_1 = \min(\mathcal{T}_{i-1,j}, \mathcal{T}_{i+1,j}) \quad \text{and} \quad \mathcal{T}_2 = \min(\mathcal{T}_{i,j-1}, \mathcal{T}_{i,j+1}),$$

the solution of (75) is equivalent to solving the following quadratic equation for $\mathcal{T}_3 = \mathcal{T}_{i,j}$

$$\left[\max\left(\frac{\mathcal{T}_3 - \mathcal{T}_1}{\Delta\chi}, 0\right)\right]^2 + \left[\max\left(\frac{\mathcal{T}_3 - \mathcal{T}_2}{\Delta\zeta}, 0\right)\right]^2 = 1.$$

Now writing $\Delta\chi = \beta\Delta\zeta$, and defining $\Delta\mathcal{T}$ and Θ as

$$\Delta\mathcal{T} = \mathcal{T}_2 - \mathcal{T}_1, \quad \Theta = \sqrt{\Delta\chi^2(1 + \beta^2) - \beta^2\Delta\mathcal{T}^2}, \tag{77}$$

we deduce the following expression for $\mathcal{T}_3$

$$\mathcal{T}_3 = \frac{\mathcal{T}_1 + \beta^2\mathcal{T}_2 + \Theta}{1 + \beta^2}. \tag{78}$$

Starting with the boundary conditions (65) defined on $\partial\mathscr{A}^c$, the crossing-time field $\mathcal{T}(\chi, \zeta)$ is now propagated to cover a narrow band that contains all points $(\chi, \zeta) \in \mathscr{A}^t$ using the fast marching method (FMM) (see [51] for a complete description of the FMM).

Having determined $\mathcal{T}_3$, it is now possible to determine a number of geometric and kinematic quantities that are required to complete the implicit algorithm. In order to determine the volume of fluid stored in a tip element (see Section 4), it is important to establish the distance ℓ between between the front and the opposite vertex of the

tip element, which can conveniently be expressed in the form

$$\ell = -\left(\frac{\mathcal{T}_1 + \mathcal{T}_2}{2}\right), \tag{79}$$

while the unit outward normal to the front is given by

$$\vec{n} = (\cos\alpha, \sin\alpha)$$
$$= \frac{1}{\Delta\chi(1 + \beta^2)}(\Theta + \beta^2\Delta\mathcal{T}, \beta(\Theta - \Delta\mathcal{T})). \tag{80}$$

Finally, the local normal front velocity can be determined from (70).

5.3. Geometric interpretation

The procedure for locating the front using the FMM [51] can readily be interpreted geometrically by reference to Fig. 7. Let us assume that both elements $(i - 1, j)$ (with central node A) and $(i, j - 1)$ (with central node B) belong to the ribbon of elements $\partial\mathscr{A}^c$ at the periphery of the channel region. We seek to determine the position of the front (given by the distance ℓ between the front and the opposite vertex O of the tip element) and its orientation (given by the angle α between the exterior normal to the front and the χ-axis), assuming that the front is currently in element i, j (with central node C).

The signed distances between the front and nodes A and B, respectively $\mathcal{T}_1$ and $\mathcal{T}_2$, are computed using (65), which rely in general on the current crack width computed at these nodes during the channel iterations, and the values of the signed distance at the same nodes at the previous time step. Assume that $\mathcal{T}_1$ is smaller than $\mathcal{T}_2$ (recalling that both quantities are negative). Within the approximation of the numerical algorithm, the level sets of the field $\mathcal{T}(\chi, \zeta)$ are parallel lines in the four element stencil sketched in Fig. 7, which also shows in dashed lines the four level sets of the field $\mathcal{T}(\chi, \zeta)$ passing through the central nodes A, B and C, and through the vertex O. Since O is equidistant from A and B, the value of the level set passing
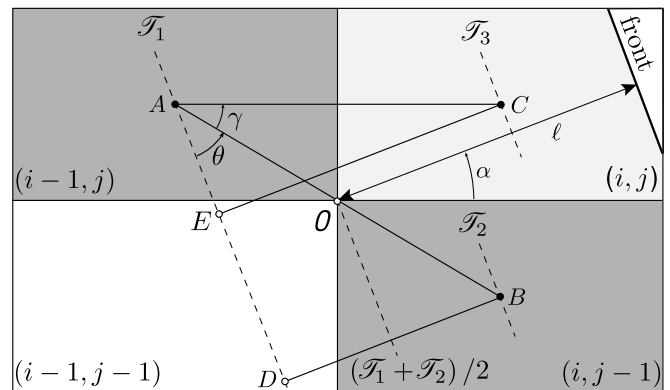

Fig. 7. Geometrical interpretation of the fast marching method.

through O is simply $(\mathcal{T}_1 + \mathcal{T}_2)/2$, which provides a simple geometric explanation of expression (79) for the length ℓ (recall that $\mathcal{T} = 0$ at the front).

The inclination α of the normal to the front is calculated as follows. From Fig. 7, it can be seen that $\alpha = \pi/2 - \gamma - \theta$, where γ is the angle $\widehat{BAC}$, an attribute of the grid, and θ is the angle $\widehat{BAD}$, with D denoting the intersection of the level set $\mathcal{T}_1$ with the normal to the front passing through node B. These two angles can be determined from simple trigonometric and geometric considerations. Indeed, $\tan\gamma = \Delta\zeta/\Delta\chi$ and $\tan\theta = \|BD\|/\|AD\|$. The distance $\|BD\|$ is the distance between the two level sets $\mathcal{T}_1$ and $\mathcal{T}_2$, i.e. $\|BD\| = \Delta\mathcal{T}$ using (77). Since $\|AB\| = (1 + \beta^2)^{1/2}\Delta\chi/\beta$, the distance $\|AD\|$ is given by

$$\|AD\| = [(1 + \beta^2)\Delta\chi^2 - \beta^2\Delta\mathcal{T}^2]^{1/2}/\beta$$

or $\|AD\| = \Theta/\beta$, using the definition (77). Hence, $\tan\gamma = 1/\beta$ and $\tan\theta = \beta\Delta T/\Theta$. It then follows that

$$\tan\alpha = \frac{\beta(\Theta - \Delta\mathcal{T})}{\Theta + \beta^2\mathcal{T}}$$

from which (80) is easily recovered.

Finally the signed distance $\mathcal{T}_3$ of node C from the front is calculated as $\mathcal{T}_3 = \mathcal{T}_1 + \|CE\|$ where E denotes the intersection of the level set $\mathcal{T}_1$ with the normal to the front passing through the central node C. Since $\|CE\| = \Delta\chi\cos\alpha$, we find in view of (80) that

$$\mathcal{T}_3 = \mathcal{T}_1 + \frac{\Theta + \beta^2\Delta\mathcal{T}}{1 + \beta^2},$$

which is equivalent to (78).

5.4. Summary of the implicit level set algorithm

To close, we briefly summarize the components of the algorithm, which starts from an initial solution that typically corresponds to one of the analytic solutions provided in Appendix C

Implicit level set algorithm for HF
  Advance time step: $\tau \leftarrow \tau + \Delta\tau$
    Start front iteration loop $k = 1 : N_f$
      Solve (63) for $\Delta\mathbf{\Omega}^c(\tau)$ and $\mathbf{\Pi}^t(\tau)$
        (starting with the old footprint $\mathscr{A}(\tau - \Delta\tau)$).
      Set BC for $\mathcal{T}$ along $\partial\mathscr{A}^c$ using (65) and
        use FMM to solve $|\nabla\mathcal{T}| = 1$.
      Use $\mathcal{T}(\chi, \zeta)$ field to locate front position and
        to compute ℓ, $\overrightarrow{n}$, and v.
      Use ℓ, $\overrightarrow{n}$, v to evaluate new estimate for the
        average
        tip widths $\mathbf{\Omega}^t(\tau)$ and the tip leak-off term $\Delta\mathscr{L}^t$
      Check for convergence $\|\mathscr{F}_k - \mathscr{F}_{k-1}\| < tol \cdot \mathscr{F}_1$,
        break
    end front iteration loop
  end time step loop

6. Numerical results

In this section we demonstrate the performance of the new implicit level set algorithm (ILSA) by comparing the numerical results to a number of analytic solutions that have been derived for radially symmetric fractures. The first class of problems deals with a crack driven either by a uniform internal pressure field or by a uniform far-field tensile stress. This problem is chosen to demonstrate that the current algorithm also works for crack problems with no fluid coupling, which probably form the vast majority of fracture growth modeling simulations [39]. The remaining examples consider fluid-driven fractures propagating in three very different regimes: toughness-storage dominated, viscosity-storage dominated, and viscosity dominated with leak-off. These specific problems have been chosen as they encapsulate some extremes of physical behavior that are encountered during hydraulic fracture propagation. Except for a particular case that deals with a far-field stress with a constant gradient, all the numerical simulations were conducted by assuming that the far-field stress is homogeneous so as to enforce an axisymmetric geometry and to enable comparison of the ILSA results either with available closed-form analytic solutions (summarized in Appendix C) or with a one-dimensional numerical solution that assumes radial symmetry.

6.1. Equilibrium solution of a penny-shaped crack

We apply the new front location algorithm to two related problems involving the propagation of a crack subject to a uniform net pressure field given by the classical limit equilibrium solution [52]. The first physical situation involves an unpressurized penny-shaped fracture in an infinite elastic medium, subject to a far-field tensile stress $-\sigma_0$ normal to the crack plane. For a given far-field stress there exists a critical radius γ_* below which the crack will not propagate and beyond which the crack will grow unstably, see for example [45]. This boundary condition is the same as that considered in [38,39], except that in that model fatigue growth due to a pulsating load was considered and growth, restricted to N loading cycles, was assumed to be governed by Paris' law. The other related problem involves the injection of a fixed volume of fluid Υ_0 of a sufficient magnitude to induce a starter crack to propagate. Without the addition of any more fluid, the crack reaches the critical radius γ_* at which the declining fluid pressure is such that the stress intensity K_I is in equilibrium with the fracture toughness K_{Ic}. It should be noted that this is in fact the solution on the K-vertex in which the fluid pressure is assumed to be hydrostatic. While the critical radius in each situation is algebraically identical, in the first situation (referred to as super-critical), the crack will propagate for any radius larger than γ_* while in the second situation (referred to as sub-critical), the crack will expand and terminate at the critical radius from any smaller initial crack.

The equations governing this class of problems are summarized in Appendix C in a form that is compatible with the scaling for fractures propagating in impermeable rocks, as described in Appendix D. Assuming a uniform net pressure field Π, the crack opening displacement $\Omega(\rho)$ and the fracture volume Υ corresponding to a crack radius γ are given by

$$\Omega = \frac{8\Pi\gamma}{\pi}\sqrt{1 - \left(\frac{\rho}{\gamma}\right)^2}, \quad \Upsilon = \frac{2^4\Pi\gamma^3}{3} \qquad (81)$$

noting also that the critical radius γ_* at which the crack is in limit equilibrium (i.e., $K_I = K_{Ic}$) is given by

$$\gamma_* = \frac{\pi^2}{2^7\Pi^2}. \qquad (82)$$

For the first problem, the crack surfaces are stress-free ($\Pi_f = 0$) while the tensile stress is prescribed to be $\varphi = -1$, so that only the elasticity Eq. (39) needs to be solved for Ω at each new fracture footprint. For the second problem characterized by $\varphi = 0$, the hydrostatic fluid pressure $\Pi_f(\tau)$, which decreases as the fracture grows, also needs to be determined. In this case the lubrication equation, because the viscous term vanishes, reduces to the following simple volume balance equation $e^T\Omega\Delta\mathscr{A} = \Upsilon_0$, where $e = [1\ldots 1]^T$ and $\Delta\mathscr{A} = \Delta\chi\Delta\zeta$ is the area of an element. Thus the coupled equations in this case are

$$\begin{bmatrix} C & -e \\ e^T & 0 \end{bmatrix}\begin{bmatrix} \Omega \\ \Pi_f \end{bmatrix} = \begin{bmatrix} 0 \\ \Upsilon_0/\Delta\mathscr{A} \end{bmatrix} \qquad (83)$$

To demonstrate the performance of the algorithm for the super-critical fracture propagation of a dry crack, in Fig. 8 we plot a sequence of fracture footprints starting with a square fracture of half-length 0.09, which exceeds the critical radius $\gamma = 0.0771$. For the numerical solution a mesh with $\Delta\chi = \Delta\zeta = 0.02$ was used. We observe that the initial square shape, which is indicated by the gray shaded elements, rapidly evolves to the appropriate radial shape. In the first time-step, the algorithm pulls the fracture front location in the corner elements of the initial square region closer to the center of the fracture in order to best approximate the current circular front – whence the apparent clustering of nodes. The circle with the solid boundary is at the critical radius γ_*.
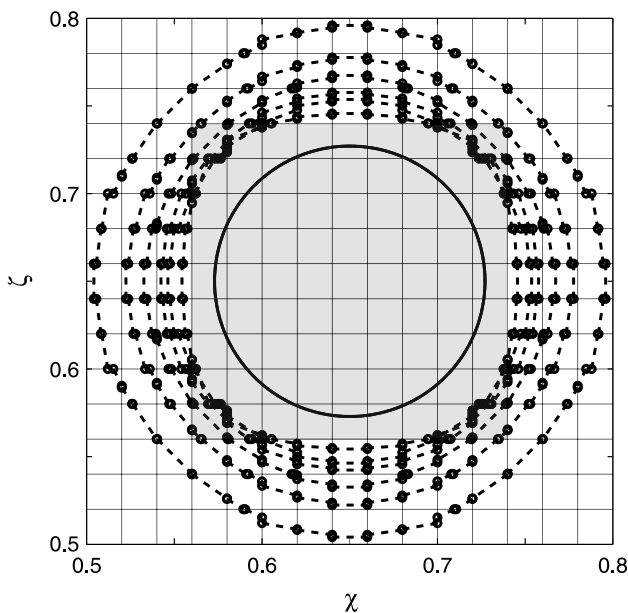
To demonstrate the subcritical propagation, we choose the critical radius to be $\gamma_* = 8$ and inject the corresponding fluid volume $\Upsilon_0 = 2^{1/2}\pi\gamma_*^{5/2}/3$ (obtained by eliminating Π between the expression for Υ in (81) and the expression for γ_* in (82) with $\Upsilon = \Upsilon_0$ and $\gamma = \gamma_*$) into a sub-critical starter crack and allow the fracture to propagate until it reaches equilibrium. This experiment tests the accuracy with which the free boundary location algorithm is able to locate the critical radius. In order to improve the accuracy provided by the piecewise constant displacement discontinuity elements, we used the edge correction procedure described in [53]. In Fig. 9 we superimpose the circular analytic solution at the critical radius with the numerical fracture footprint using $\Delta\chi = \Delta\zeta = \frac{1}{2}$. The footprint of the starter crack is shown in the interior of the critical fracture footprint.

6.2. Toughness-dominated hydraulic fracture propagation

In this example we consider a circular hydraulic fracture propagating close to the K-vertex in an impermeable medium so that $C' = 0$.

Fig. 8. Sequence of fracture footprints starting with a square fracture of half-length 0.09 units indicated by the shaded region, which exceeds the critical radius $\gamma_* = 0.0771$ (supercritical case).
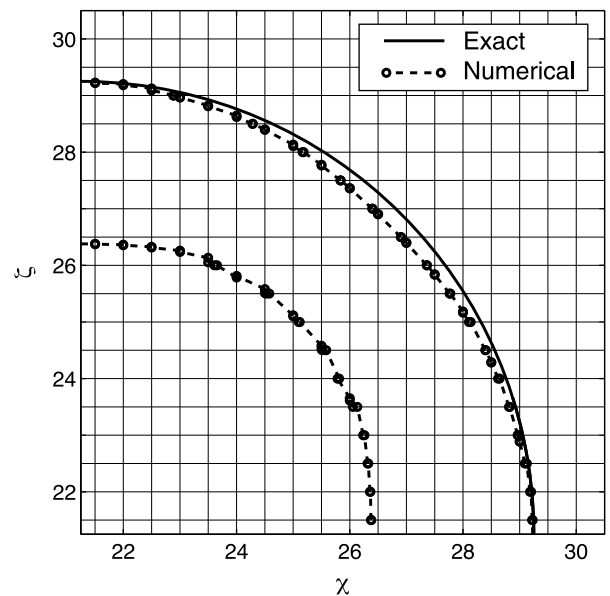
Fig. 9. Comparison between the penny-shaped fracture at the critical radius $\gamma_* = 8$ with the numerical fracture footprint using $\Delta\chi = \Delta\zeta = \frac{1}{2}$. The subcritical starter crack is also shown.

6.2.1. Comparison with analytical solution

For the first simulation we assume that $\Delta\chi = \Delta\zeta = 3.14$, and start with a crack of radius $\gamma = 13.52$, which corresponds to a dimensionless time $\tau = 1135.44$ according to the analytical solution summarized in Appendix C. The time step $\Delta\tau = 223.15$ was chosen to correspond to an initial front advance of approximately one element at a time. In Fig. 10 we superimpose on the square computational grid the first quadrant portions of the fracture footprints corresponding to a selection of times τ ranging from 1135.44 to 23003.90. The intersection poi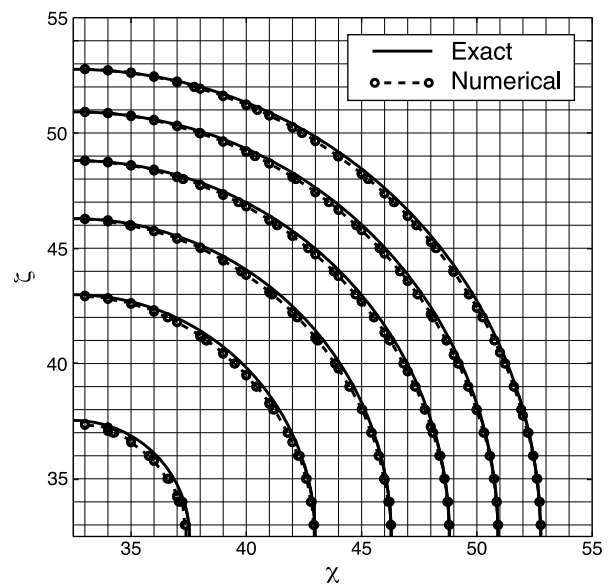nts between the numerical fronts and the grid lines are indicated by open circles. The close agreement between the numerical and analytic fronts clearly demonstrates the accuracy with which the implicit level set algorithm locates the front posi-

tions. In Fig. 11 we compare the time evolution of the average numerical fracture radius over all the tip elements with the analytic solution $\gamma(\tau)$. We compare the numerical and analytic width profiles for the last time step of the computation $\tau = 23003.90$ in Fig. 12 and the numerical and analytic pressure profiles at the same time horizon in Fig. 13. There is remarkably good agreement between these numerical and analytic solutions given the coarseness of the mesh.

6.2.2. Convergence study

In order to explore the convergence properties of the implicit level set algorithm, we evolve a starter crack having an initial radius $\gamma = 68.04$ at time $\tau = 58106.52$ for only 20 time steps of magnitude $\Delta\tau = 4220.60$, using three different mesh sizes $\Delta\chi = 4$, 8 and 16. From Fig. 14 it can be seen that average radii of the three numerical approximations clearly converge to the exact solution as the mesh is refined. The asymptotic convergence rate of the mean tip radius over this time period is given by $\|\gamma_{ave}(\tau) - \gamma_{ex}(\tau)\|_2 = O(\Delta\chi^p)$ where $p \simeq 1.3$ as can be seen from Fig. 15. In Fig. 16 we illustrate
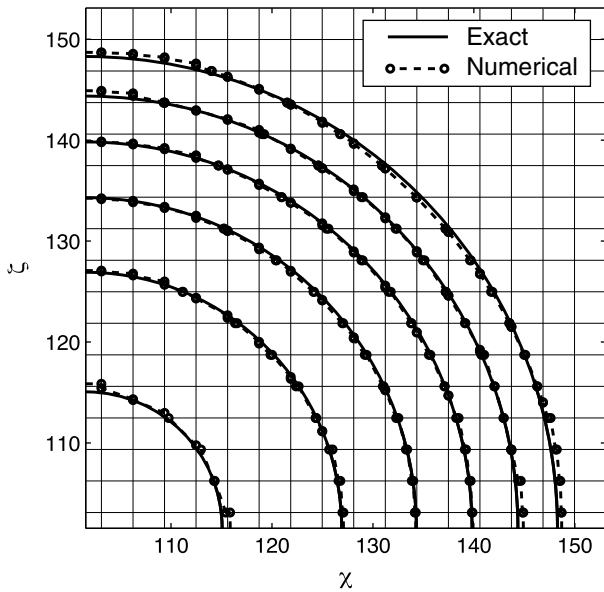
Fig. 10. First quadrant projections of the fracture footprints that correspond to times $\tau = [1135.44, 5152.10, 9615.05, 14078.00, 18540.95, 23003.90]$ along with the square grid that was used in the computations.

Fig. 12. Comparison between the numerical and analytic width profiles for the last time step of the computation $\tau = 23003.90$.
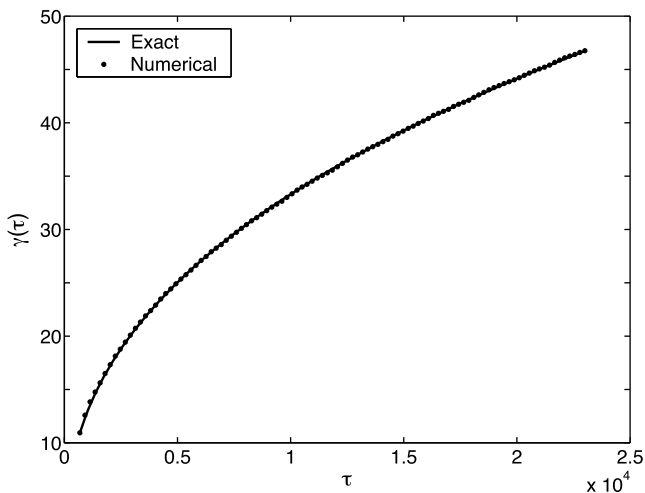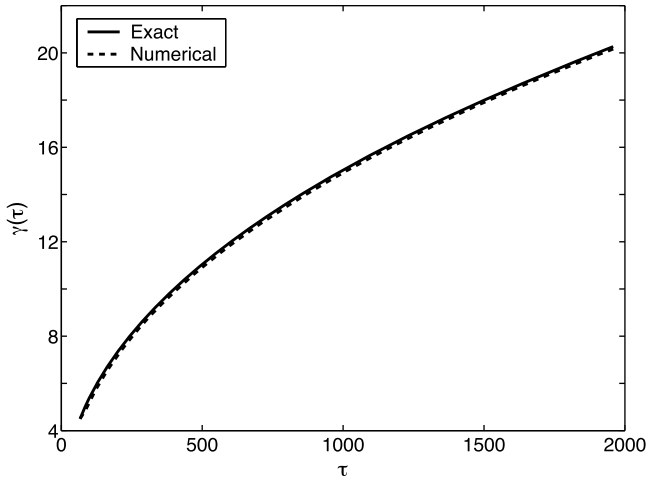

Fig. 11. Comparison between the time evolution of the average numerical fracture radius over all the tip elements and the analytic solution $\gamma(\tau)$.
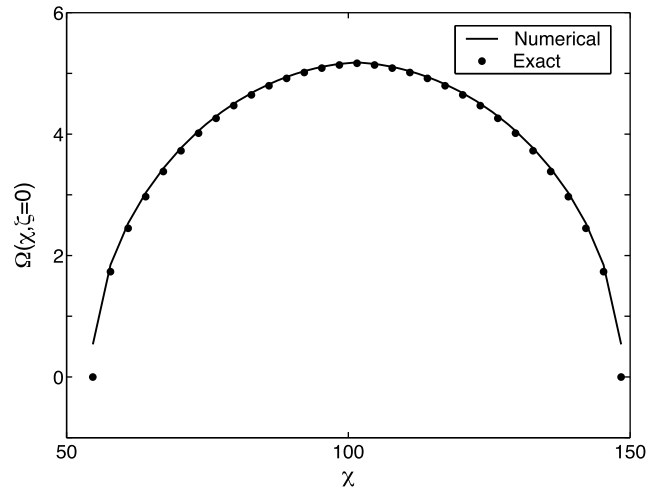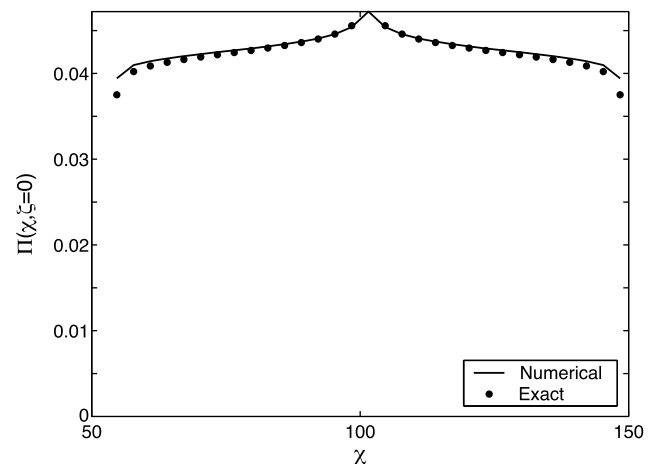
Fig. 13. Comparison between the numerical and analytic pressure profiles for the last time step of the computation $\tau = 23003.90$.
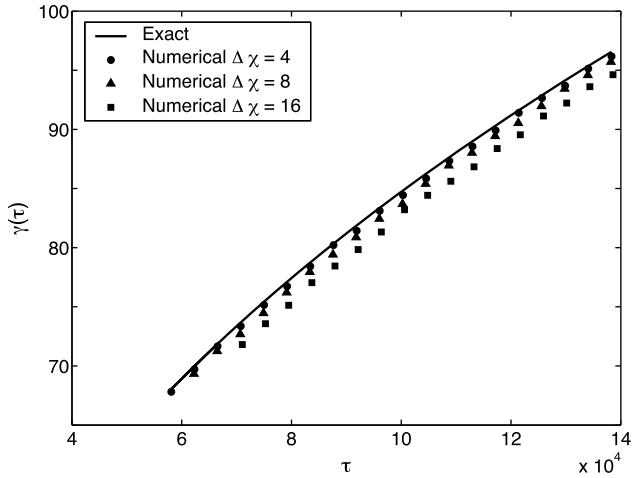
Fig. 14. Plot showing convergence of the average radii of three numerical approximations to the exact solution.
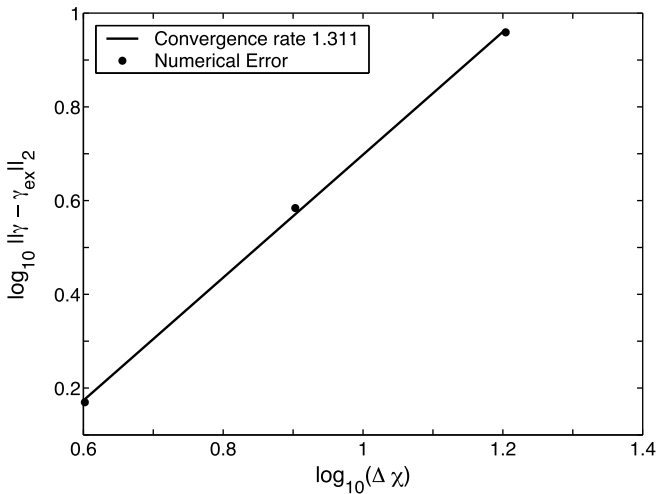
Fig. 15. Plot showing convergence rate of the mean tip radius to the exact radius.
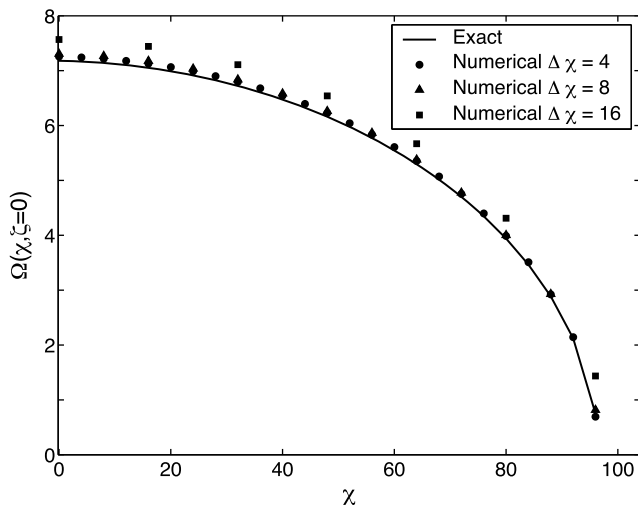
Fig. 16. Plot showing convergence of the fracture width to the exact solution.

the convergence of the numerical fracture widths Ω evaluated at the last time step to the exact solution as the mesh $\Delta\chi$ is refined. The average convergence rate of the weighted l_2 norm of the width, defined by $\|\mathbf{\Omega}(\tau) - \mathbf{\Omega}^{\text{ex}}(\tau)\|_2^2 = \frac{1}{N}\sum_{k=1}^{N}(\Omega_k(\tau) - \Omega_k^{\text{ex}}(\tau))^2$, over all time steps in the simulation is 1.1. It should be noted that piecewise constant displacement discontinuity approximation has been shown to be only first order accurate [53], so we could not expect this convergence rate to be any better than unity.

6.3. Viscosity-dominated hydraulic fracture propagation

Here we consider a hydraulic fracture propagating in an impermeable medium which has no toughness so that $C' = 0$ and $K' = 0$. Two situations are analyzed with regard to the far-field stress: (i) a homogeneous *in situ* stress leading to the development of a radially symmetric fracture; (ii) an *in situ* stress characterized by a constant gradient.

6.3.1. Homogeneous in situ stress

This situation corresponds to a radial hydraulic fracture propagating at the *M*-vertex, for which there is an analytical solution [54], see Appendix C.

In the first experiment, we assume that $\Delta\chi = \Delta\zeta = 1$ and start with a crack of radius $\gamma = 4.5$, which corresponds to a dimensionless time $\tau = 66.32$ according to the power law solution for the *M*-vertex. A time step $\Delta\tau = 18.92$ was chosen so that the initial front advances approximately one element per step. In Fig. 17 we superimpose on the computational grid the first quadrant projections of the fracture footprints that correspond to a selection of times τ ranging from 85.24 to 1958.56. The intersection points between the numerical fronts and the grid lines are indi-

Fig. 17. *M*-vertex solution. First quadrant projections of the fracture footprints that correspond to times $\tau = [85.24, 444.76, 823.21, 1201.66, 580.11, 1958.56]$ along with the square grid that was used in the computations.

Fig. 18. Comparison between the time evolution of the average numerical fracture radius over all the tip elements and the analytic solution $\gamma(\tau)$.

cated by open circles. The close agreement between the numerical and analytic fronts, which improves as time evolves, clearly demonstrates the accuracy with which the implicit level set algorithm locates the front positions. In Fig. 18 we compare the time evolution of the average numerical fracture radius over all the tip elements with the analytic solution $\gamma(\tau)$. The numerical solution underestimates the exact solution, which a convergence study (not presented) demonstrates is due to the spatial discretization error.

The normal velocity of the front can be determined by the implicit level set algorithm using (70). In Fig. 19 we provide a trace of the computed front speed for the tip element located at $(\chi, \zeta) \simeq (\gamma, 0)$, the average normal front velocity over all the tip elements, and the exact normal velocity of the front. The oscillations about the analytic velocity for the individual tip element trace can be explained by the fluctuations in the approximation introduced by the fixed
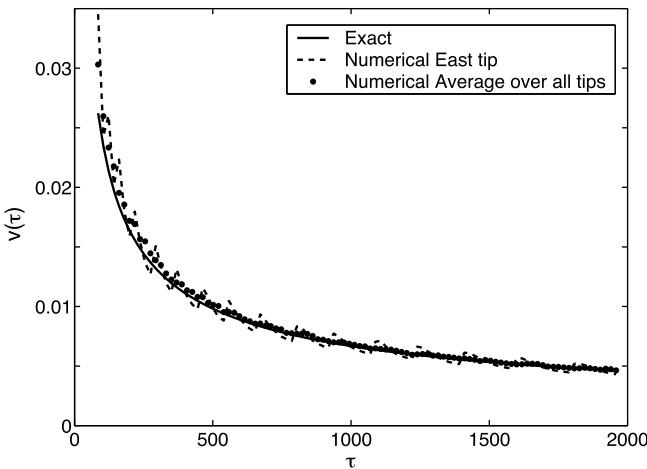
Fig. 19. The exact normal velocity of the front, the trace of the computed front speed for the tip element located at $(\chi, \zeta) \simeq (\gamma, 0)$, and the average normal front velocity over all the tip elements.
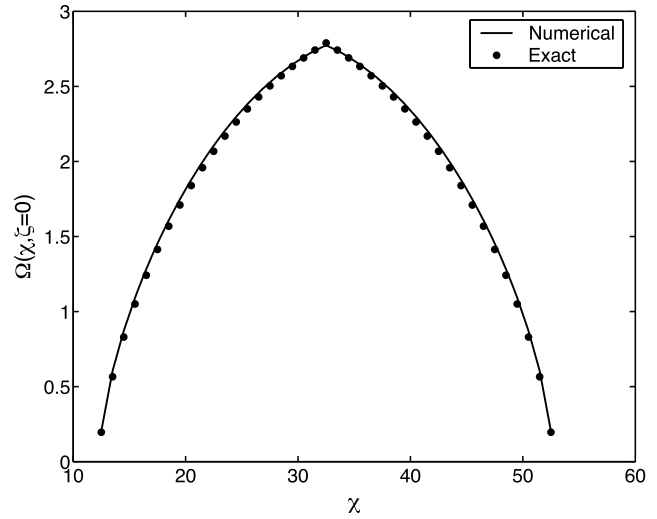
Fig. 20. Comparison between the numerical and analytic width profiles for the last time step of the computation $\tau = 1958.56$.
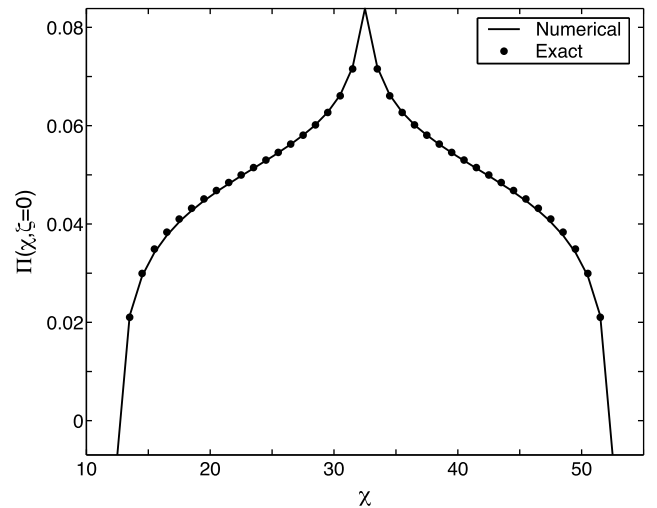
Fig. 21. Comparison between the numerical and analytic pressure profiles for the last time step of the computation $\tau = 1958.56$.

Eulerian mesh. The smoother average front velocity is to be expected due to the fact that volume balance is maintained for each step of the computation. We compare the numerical and analytic width profiles for the last time step of the computation $\tau = 1958.56$ in Fig. 20 and the corresponding numerical and analytic pressure profiles in Fig. 21 There is remarkably good agreement between the numerical and analytic solutions given the coarseness of the mesh.

6.3.2. Linear variation of the in situ stress

In this case we consider the propagation of a viscosity-dominated hydraulic fracture in a medium subject to an *in situ* stress field σ, assumed to vary linearly with ζ according to
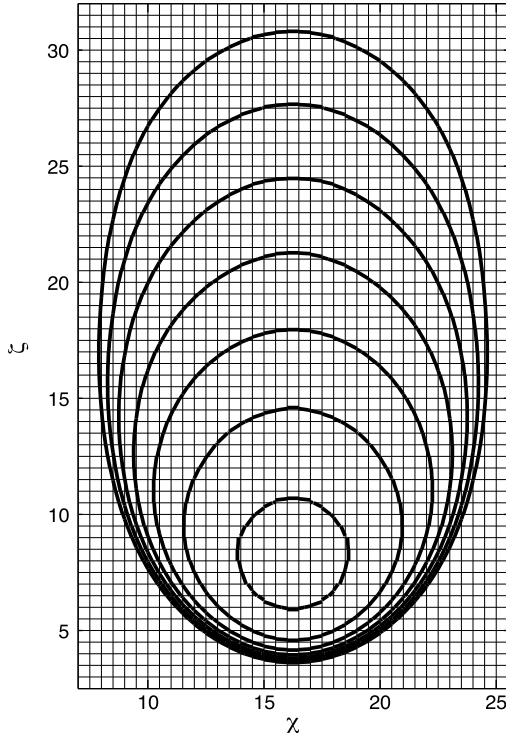
Fig. 22. Successive footprints of a hydraulic fracture propagating in the storage-viscosity regime ($K' = C' = 0$), in the presence of an *in situ* stress field σ characterized by a constant vertical stress gradient.

$$\varphi(\chi, \zeta) = \frac{(\zeta_M - \zeta)}{(\zeta_M - \zeta_m)},$$

where $\zeta_m = 0.25$ and $\zeta_M = 32.25$ are the minimum and maximum ζ coordinates on the Eulerian mesh and φ is defined in (16). We use a mesh with $\Delta\chi = \Delta\zeta = \frac{1}{2}$, a time step $\Delta\tau = 3.18$, and assume a pumping rate defined by $\psi(\tau) = 1$. In Fig. 22 we plot successive fracture footprints starting from an initial fracture that is given by the M-vertex radially symmetric solution. The fracture grows preferentially upward into the regions of lower resistance while the downward growth is virtually halted by the increase in confinement. It is interesting to note that this situation is equivalent to the growth of a buoyancy-driven hydraulic fracture [55,56].

6.4. Hydraulic fracture propagation along the $M\widetilde{M}$-edge

Finally we simulate the propagation of an axisymmetric hydraulic fracture under conditions where $K' = 0$ and $C' > 0$. Evolution of such a fracture corresponds to a transition along the $M\widetilde{M}$-edge of phase space, from the small-time M-vertex asymptotics towards the large-time $\widetilde{M}$-vertex asymptotics. Since an analytic solution to this problem is not yet available, we compare the numerical solution obtained using the implicit level set algorithm with a one-dimensional numerical solution EMMA that exploits radial symmetry [29]. Both the small and large time asymptotics are listed in Appendix C.

For this simulation, we have assumed that the opening in the tip element always corresponds to the $\tilde{m}$ solution,

i.e., $\Omega \sim 2^{1/4}\beta_{\tilde{m}0}v^{1/8}\xi^{5/8}$ as $\xi \to 0$, as the generalized $m\tilde{m}$ asymptote presented in Section 3 has not yet been implemented. This approximation introduces an error in the magnitude of tip opening, which can reach about 25% at early time. Indeed, the tip velocity must drop below the critical value $v_{\tilde{m}}$ given by (see Section 3)

$$v_{\tilde{m}} = \left(\frac{64\xi_{\tilde{m}}}{\Delta\zeta}\right)^{1/5} \tag{84}$$

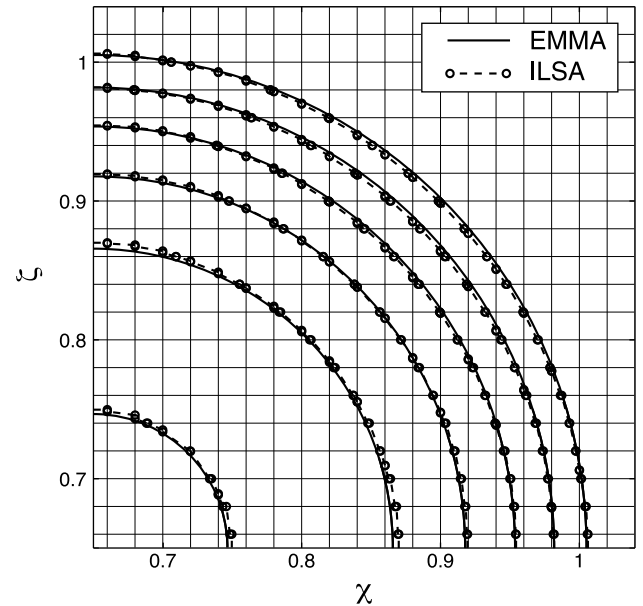for the tip element to be fully within the $\tilde{m}$-asymptotic umbrella (assuming a square grid). For the grid size

Fig. 23. Fracture propagation along the $M\widetilde{M}$ edge. First quadrant projections of the fracture footprints that correspond to times $\tau = [0.0173, 0.1563, 0.2980, 0.4397, 0.5815, 0.7232]$ along with the square grid used in the computations and comparison with radius obtained with the algorithm EMMA.
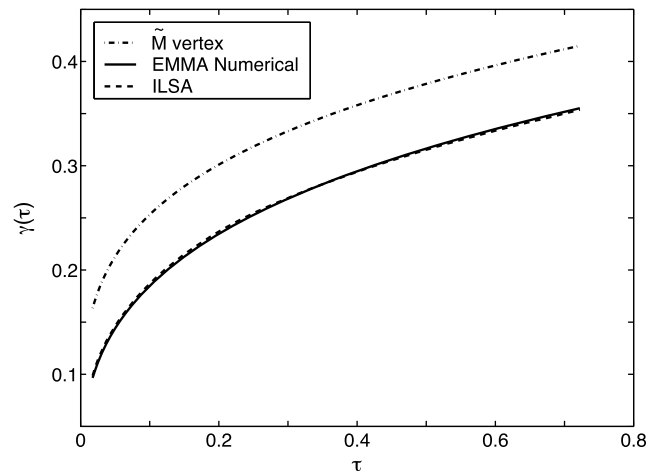

Fig. 24. Comparison between the time evolution of the average numerical fracture radius over all the tip elements and the one-dimensional numerical EMMA solution $\gamma(\tau)$. The large time $\widetilde{M}$-solution is also plotted in this figure.

$\Delta\chi = \Delta\zeta = 0.02$ used in this simulation, $v_{\tilde{m}} \simeq 0.13$, which is only reached near the end of this simulation.

The numerical simulation starts with a crack of radius $\gamma = 0.09$, which corresponds to a dimensionless time $\tau = 0.0145$ according to the M-vertex solution, and uses a time step $\Delta\tau = 0.0028$. In Fig. 23 we compare the footprints corresponding to sample times τ in the range [0.0173,0.7232] generated by the implicit level set algorithm ILSA with those obtained using EMMA. As with the other propagation regimes, there is close agreement between the two solutions. In Fig. 24 we plot the fracture radius $\gamma(\tau)$ obtained using EMMA (solid), which shows close agreement to the average fracture radius calculated by ILSA (dashed line). Also plotted in this figure is the fracture radius for the $\widetilde{M}$-vertex solution to which the above two solutions will tend for $\tau \gg 1$. In Fig. 25 we compare the tip velocity calculated using EMMA with the ILSA velocity for a single tip element (dashed) as well as the normal velocity averaged over all tip elements (solid circles). Initially ILSA over-estimates the tip velocity, but this value rapidly converges to that obtained using EMMA. We observe minor fluctuations in the ILSA velocity trace of the individual tip element, which are correlated to the times at which the front transitions from one rectangular element to the next, but these fluctuations are smoothed out in the normal velocities that are averaged over all the tip elements. There is good agreement between the two algorithms for both the fracture width and the net pressure, as evidenced in Figs. 26 and 27.

As a global measure of the amount of leak-off that has occurred over the evolution of a fracture, it is common to define the efficiency as follows

$$\mathscr{E}(\tau) = \frac{\int_{\mathscr{A}} \Omega(\chi, \zeta, \tau) \mathrm{d}\mathscr{A}}{\int_0^\tau \psi(\tau') \mathrm{d}\tau'}.$$

In Fig. 28 we compare the efficiency $\mathscr{E}(\tau)$ (expressed as a percentage) calculated using ILSA to that obtained with
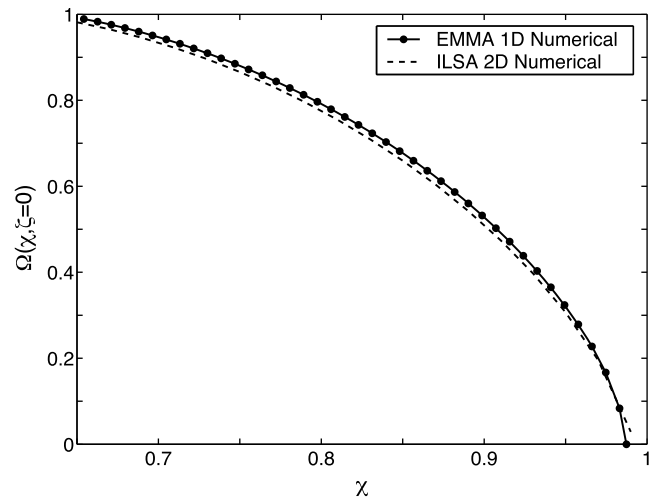

Fig. 26. Comparison between the ILSA and EMMA width profiles for $\tau = 0.7232$.
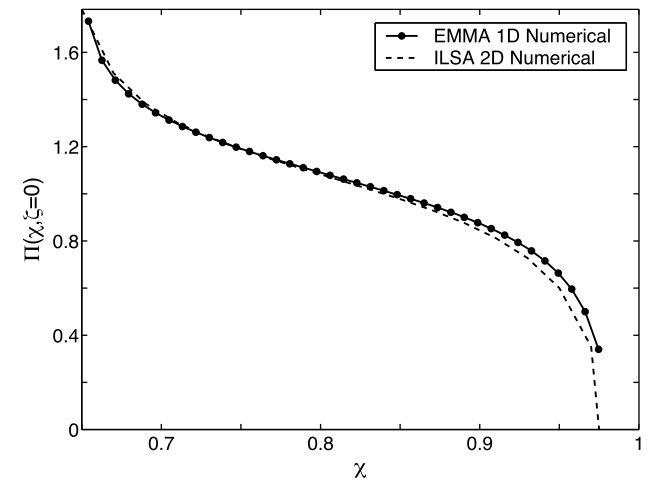

Fig. 27. Comparison between the ILSA and EMMA pressure profiles for $\tau = 0.7232$.
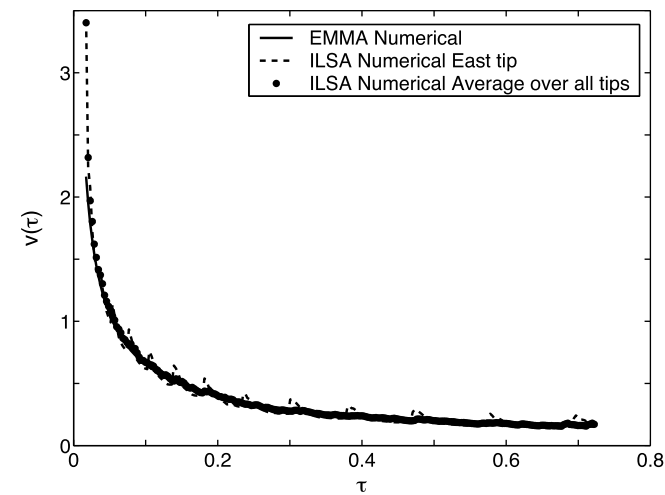

Fig. 25. The normal velocity of the front computed with EMMA, the trace of the computed front speed for the tip element located at $(\chi, \zeta) \simeq (\gamma, 0)$, and the average normal front velocity over all the tip elements.
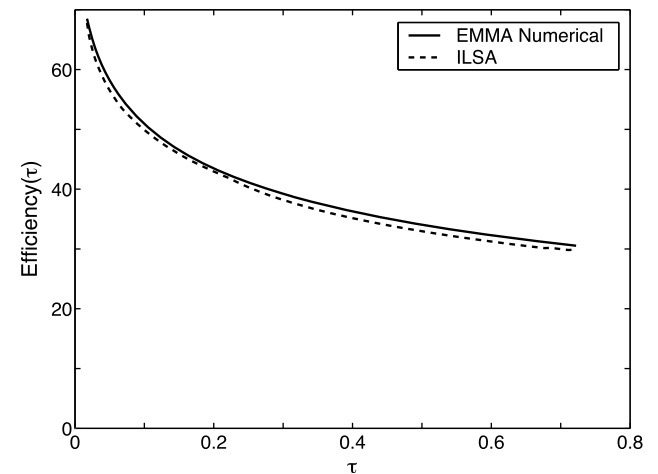

Fig. 28. Comparison between the evolution of the fracture efficiency computed with ILSA and EMMA.

EMMA. Since the integrands in (44) both have negative curvatures, the midpoint rule used in ILSA will over-estimate these integrals, which will lead to leak-off terms in Γ that are slightly too large. As a result the implicit level set algorithm ILSA will allow slightly too much fluid to leak into the surrounding medium, resulting in estimates of the efficiency that are slightly lower than those given by EMMA.

7. Conclusions

In this paper we have presented a novel implicit level set algorithm for resolving the free boundary problem associated with the propagation of hydraulic fractures. A number of characteristics of the HF governing equations and their coupling present considerable challenges for numerical modeling, namely: the degenerate lubrication equation, the hypersingular non-local elasticity equation, and the indeterminate form of the velocity of the unknown fracture front. An implicit algorithm is necessary for the efficient solution of the stiff evolution equations that involve fully populated matrices associated with the coupled non-local elasticity and degenerate lubrication equations. Recent asymptotic analyses have identified the multi-scale structure of the HF propagation problem with different length and time scales corresponding to competing physical processes such as: the competition between the energy loss due to viscous dissipation and the energy released in breaking the rock; and the competition between storage of fluid in the fracture and leak-off of fluid. In this paper, we demonstrate that close to the tip of an arbitrarily shaped fracture with a smooth front, the governing equations reduce to those for a semi-infinite hydraulic fracture propagating at a constant speed. Thus, in the vicinity of the tip, the form of the solution even for an arbitrarily shaped fracture is given by one of the similarity solutions that can be obtained by asymptotic analysis.

This observation presents the opportunity to substantially improve the accuracy of numerical HF approximations, while consuming modest computational resources, by incorporating the asymptotic behavior of the solution close to the tip. Achieving this objective has hitherto proved elusive due to the difficulty of implementing arbitrary power law tip shape functions in the approximation of the elasticity equation and the fact that determining the velocity field requires the evaluation of an indeterminate form. The implicit level set algorithm described in this paper makes it possible to use the tip asymptotic solution to locate the evolving free boundary without requiring that the tip velocity be specified *a priori* or evaluated using pressure gradients. Indeed, the front velocity is determined as a by-product of the implicit level set algorithm. The tip asymptotic solution is implemented in a weak form involving average widths at the centres of piecewise constant DD elements, while the corresponding tip pressures, consistent with mass balance, are determined by solving a mixed-variable system of non-linear equations by fixed-point itera-

tion. The accuracy of this approach is due to the fact that only the fracture width field, which is continuous, is used to locate the free boundary. By contrast, alternative methods involve first evaluating the velocity field using the singular pressure gradients and then using an existing method for locating the free boundary such as front tracking, the VOF method, or the standard level set algorithm.

The implicit level set algorithm described in this paper involves a boundary value problem for the Eikonal equation in which the boundary values for the crossing-time function $\mathscr{T}(\chi, \zeta)$ are established by inverting the tip asymptotic relation. This formulation differs from the standard boundary value level set algorithm in the following respects: the velocity field is not required; it is not necessary to update the signed distance function periodically; it is not necessary to determine an extension velocity field; and the method will apply to advancing or receding fractures, provided the appropriate tip asymptotic solution has been determined. Finally, we note that the precision with which we are able to locate the fracture front has a critical effect on the accuracy of the numerical solution. Indeed, associated with each fracture footprint that is a small perturbation of the actual footprint, there is a pair of equilibrating and volume preserving widths and pressures. Thus among this multiplicity of solutions, it is imperative that the free boundary location algorithm select the appropriate footprint that matches the propagation condition, and which corresponds to a solution to the elastic force equilibrium equation and the lubrication volume balance equation.

In this paper we provide a number of numerical comparisons with radially symmetric analytical solutions that have been derived for spatially homogeneous problems under a variety of propagation regimes: a fracture subjected to a constant pressure field; toughness-storage-dominated propagation; viscosity-storage-dominated propagation; and viscosity-dominated propagation with leak-off. The numerical solutions obtained using the novel implicit level set algorithm show close agreement with the reference solutions. The algorithm is able to locate the free boundary with first order accuracy, while the corresponding width field is approximated with the first order accuracy expected of the piecewise constant displacement discontinuity method. As an illustration, the algorithm is also applied to a symmetry-breaking *in situ* confinement field, which is equivalent to a buoyancy-driven fracture. These examples clearly establish the accuracy and robustness of the novel implicit level set algorithm in the numerical solution of hydraulic fractures in a variety of regimes.

Appendix A. Particular integral over the tip region

We are interested in computing the integral $I(\ell)$ defined as

$$I(\ell) = \int_{\Delta \mathscr{A}_\ell} g \, \mathrm{d}\mathscr{A}, \tag{A.1}$$

where $\Delta \mathscr{A}_\ell$ is the fluid-filled part of a tip element (represented by the gray fill in Fig. 6). The domain $\Delta \mathscr{A}_\ell$ is bounded by edges or part of edges of the tip element and by the (straight) fluid front with external unit normal $(\cos\alpha, \sin\alpha)$. The peculiarity of the integral $I(\ell)$, which we exploit in this calculation, is that the integrand g is only a function of the distance from the front.

Let ℓ denote the distance the front has propagated into the element from its point of entry (the vertex at the intersection of edges 1 and 4 in the example shown in Fig. 6), and let ξ denote the coordinate along an axis perpendicular to the front and with its origin on the front; ξ is positive for points located inside the flow domain. The integrand $g(\xi)$, defined over $0 \leqslant \xi \leqslant \ell$, is assumed to be continuous for $\xi > 0$ and to be at most weakly singular at $\xi = 0$. Under these conditions, we show that the integral $I(\ell)$ can be evaluated simply.

Let $G(\xi)$ denote the definite integral of g

$$G(\xi) = \int_0^\xi g(u)\,\mathrm{d}u, \tag{A.2}$$

then $I(\ell)$ can be rewritten as

$$I(\ell) = \int_{\Delta \mathscr{A}_\ell} \frac{\mathrm{d}G}{\mathrm{d}\xi}, \mathrm{d}\mathscr{A} \tag{A.3}$$

which, after application of Gauss theorem as in (52), can be expressed as

$$I(\ell) = \int_{\Delta \mathscr{C}_\ell} G n_\xi \, \mathrm{d}\mathscr{C}, \tag{A.4}$$

where n_ξ denotes the component along the ξ-axis of the unit normal to the contour $\Delta \mathscr{C}_\ell$ enclosing the flow domain $\mathscr{A}_\ell$. Since $G(0) = 0$, $I(\ell)$ can also be expressed as

$$I(\ell) = \int_{\Delta \mathscr{C}_\ell^*} G n_\xi \, \mathrm{d}\mathscr{C}, \tag{A.5}$$

where $\Delta \mathscr{C}_\ell^*$ is $\Delta \mathscr{C}_\ell$ minus the front.

Table A.1
Evaluation of $n_\xi \mathrm{d}\mathscr{C}$ for each side of the element

Edge	n_ξ	$\mathrm{d}\mathscr{C}$	$n_\xi \mathrm{d}\mathscr{C}$
1	$\sin\alpha$	$-\mathrm{d}\xi/\cos\alpha$	$-\mathrm{d}\xi \tan\alpha$
2	$-\cos\alpha$	$-\mathrm{d}\xi/\sin\alpha$	$\mathrm{d}\xi \cot\alpha$
3	$-\sin\alpha$	$\mathrm{d}\xi/\cos\alpha$	$-\mathrm{d}\xi \tan\alpha$
4	$\cos\alpha$	$\mathrm{d}\xi/\sin\alpha$	$\mathrm{d}\xi \cot\alpha$

The expression for $n_\xi \mathrm{d}\mathscr{C}$ corresponding to each edge of the rectangular element as a function of $\mathrm{d}\xi$ and α, assuming counterclockwise traversal of the element boundary is tabulated in Table A.1 (see Fig. 6 for the numbering of edges).

There are three possible cases which depend on the comparison between ℓ and the two lengths, λ and ξ_0, which are both functions of α. The length λ represents the maximum value of ℓ; i.e., λ is the maximum distance that can be travelled by the front within the element if its direction of propagation remains unchanged. By simple projection, it can be shown that

$$\lambda = \Delta\chi \cos\alpha + \Delta\zeta \sin\alpha. \tag{A.6}$$

The geometrical meaning of ξ_0, given by

$$\xi_0 = \begin{cases} \Delta\zeta \sin\alpha, & 0 \leqslant \tan\alpha \leqslant \Delta\chi/\Delta\zeta, \\ \Delta\chi \cos\alpha, & \Delta\chi/\Delta\zeta \leqslant \tan\alpha < \infty \end{cases} \tag{A.7}$$

is illustrated in Fig. 6. The three generic cases that lead to different expressions for $I(\ell)$ are described below.

(1) $0 \leqslant \ell \leqslant \xi_0$ (the front intersects edges 1 and 4). In this case

$$I(\ell) = (\cot\alpha + \tan\alpha) \int_0^\ell G(\xi)\,\mathrm{d}\xi \tag{A.8}$$

or

$$I(\ell) = m\Gamma(\ell), \tag{A.9}$$

where

$$\Gamma(\xi) = \int_0^\xi G(u)\,\mathrm{d}u, \quad m = \frac{1}{\cos\alpha \sin\alpha}. \tag{A.10}$$

(2) $\xi_0 \leqslant \ell \leqslant \lambda - \xi_0$ (the front intersects edges 1 and 3). In this case

$$I(\ell) = m[\Gamma(\ell) - \Gamma(\ell - \xi_0)]. \tag{A.11}$$

(3) $\lambda - \xi_0 \leqslant \ell \leqslant \lambda$ (the front intersects edges 2 and 3). In this case

$$I(\ell) = m[\Gamma(\ell) - \Gamma(\ell - \xi_0) - \Gamma(\ell + \xi_0 - \lambda)]. \tag{A.12}$$

(4) $m = \infty$. In this case

$$I(\ell) = \Delta\eta G(\ell), \tag{A.13}$$

where $\Delta\eta$ is equal to $\Delta\chi$ if $\alpha = \pm\pi/2$ and to $\Delta\zeta$ if $\alpha = 0, \pi$.

This procedure can be repeated for an interior element for which the fluid front as already passed, i.e. for which $\ell > \lambda$. In this case the corresponding integral:

$$J(\ell) = (\cot\alpha + \tan\alpha) \int_0^\lambda G(\xi)\,\mathrm{d}\xi$$

can be expressed in the following form:

$$J(\ell) = m[\Gamma(\ell) - \Gamma(\ell - \xi_0) - \Gamma(\ell + \xi_0 - \lambda) + \Gamma(\ell - \lambda)].$$

Appendix B. Expansion of elasticity and lubrication equations near the tip

In this appendix, we show that, in the vicinity of the fracture edge, the general elasticity Eq. (3) and the lubrication Eqs. (4)–(6) degenerate to (27). However, we perform the expansion of the equations directly in terms of the dimensionless variables and quantities. For the expansion, we introduce the system of coordinates (ξ, η) centered at point O on the fracture edge $\mathscr{C}$, with the ξ-axis normal to $\mathscr{C}$ and pointing inside the fracture domain, see Fig. 29. Since the fracture front $\mathscr{C}$ is evolving, the point O is moving at a velocity v, which is pointing in the same direction as the outward normal to $\mathscr{C}$ at O, i.e., in opposite direction to ξ. (In this paper we consider only the case where the fracture is growing, i.e., the front $\mathscr{C}$ at time τ encompasses all previous configurations of the front.)

B.1. Elasticity

First we rewrite the elasticity integral on the right-hand side of (20) in terms of a system of coordinates (ξ, η); thus

$$I(\xi, \eta) = \int_0^a \int_{\eta_l(\xi')}^{\eta_u(\xi')} \frac{\Omega(\xi', \eta')\mathrm{d}\eta'\mathrm{d}\xi'}{[(\xi' - \xi)^2 + (\eta' - \eta)^2]^{3/2}}, \tag{B.1}$$

where the bounds a, η_l, η_u, which implicity describe the geometry of the fracture edge $\mathscr{C}$, depend on the position of the origin O of the coordinate system on $\mathscr{C}$. We are interested in determining the asymptotic expansion $I_0(\xi)$ of the integral $I(\xi, \eta)$ when $\xi \to 0$ and $\eta = 0$, i.e.,

$$I_0(\xi) \overset{\xi \to 0}{\sim} I(\xi, 0). \tag{B.2}$$

In the neighbourhood of O, the front $\mathscr{C}$ has a local radius of curvature ρ; hence $\mathscr{C}$ in the vicinity of O is described by

$$(\xi - \rho)^2 + \eta^2 = \rho^2, \quad \xi/\rho \to 0, \quad \eta/\rho \to 0. \tag{B.3}$$

It follows therefore that for $\xi/\rho \to 0$, the two inner bounds $\eta_l(\xi)$ and $\eta_u(\xi)$ of the integral $I(\xi, \eta)$ can be simplified as

$$\eta_l(\xi) \sim -\sqrt{2\xi\rho}, \quad \eta_u(\xi) \sim \sqrt{2\xi\rho}, \quad \xi/\rho \to 0. \tag{B.4}$$
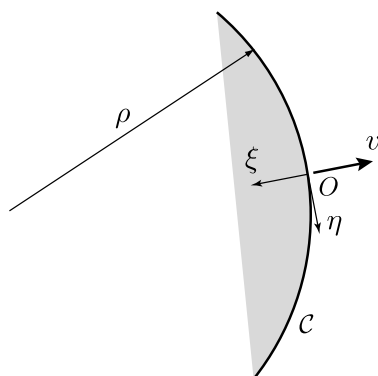

Fig. 29. Details of the fracture front for the tip asymptotics.

Now consider the asymptotic form of the inner integral $i(\xi, \xi')$ in (B.1)

$$i(\xi, \xi') = \int_{\eta_l(\xi')}^{\eta_u(\xi')} \frac{\Omega(\xi', \eta')\mathrm{d}\eta'}{[(\xi' - \xi)^2 + (\eta' - \eta)^2]^{3/2}}, \tag{B.5}$$

when $\xi/\rho \to 0$. After first expressing the integration variables ξ' and η' as

$$\xi' = u\xi, \quad \eta' = v\xi, \tag{B.6}$$

$i(\xi, \xi')$ can be rewritten as

$$i(\xi, \xi') = \xi^{-2}g(\xi, \xi'), \tag{B.7}$$

where

$$g(\xi, \xi') = \int_{\eta_l(u\xi)/\xi}^{\eta_u(u\xi)/\xi} \frac{\Omega(u\xi, v\xi)\mathrm{d}v}{[(u - 1)^2 + v^2]^{3/2}}. \tag{B.8}$$

Hence, in view of (B.4),

$$g(\xi, \xi') \overset{\xi/\rho \to 0}{\sim} \int_{-\sqrt{2u\rho/\xi}}^{\sqrt{2u\rho/\xi}} \frac{\Omega(u\xi, v\xi)\mathrm{d}v}{[(u - 1)^2 + v^2]^{3/2}}. \tag{B.9}$$

Since the crack front is a level set of the function Ω, i.e, $\Omega = 0$, any variation of the function Ω in the close vicinity to the crack front takes place in the direction normal to the front. In other words,

$$\Omega(u\xi, v\xi) \sim \Omega_s(u\xi), \quad \xi \to 0, \tag{B.10}$$

where Ω_s is used to denote an asymptotic form of the function Ω. Hence, recalling Eq. (B.4), we can write that

$$g(\xi, u\xi) \overset{\xi/\rho \to 0}{\sim} \Omega_s(u\xi) \int_{-\infty}^{\infty} \frac{\mathrm{d}v}{[(u - 1)^2 + v^2]^{3/2}}$$
$$= \frac{2\Omega_s(u\xi)}{(u - 1)^2}, \tag{B.11}$$

which leads to

$$I_0(\xi) \overset{\xi/\rho \to 0}{\sim} 2 \int_0^a \frac{\Omega_s(\xi')\mathrm{d}\xi'}{(\xi' - \xi)^2}. \tag{B.12}$$

Therefore, by taking the limit for $\xi \to 0$, we have effectively reduced the planar integral elasticity equation to the corresponding plane strain equation. After an integration by parts and noting that $\Omega_s(0) = \Omega_s(a) = 0$, we obtain

$$I_0(\xi) \overset{\xi/\rho \to 0}{\sim} 2 \int_0^a \frac{\mathrm{d}\widehat{\Omega}(\xi')}{\mathrm{d}\xi'} \frac{\mathrm{d}\xi'}{\xi' - \xi}, \tag{B.13}$$

which can readily be rewritten as

$$I_0(\xi) \overset{\xi/\rho \to 0}{\sim} 2 \int_0^{a/\xi} \frac{\mathrm{d}\widehat{\Omega}(z)}{\mathrm{d}z} \frac{\mathrm{d}z}{\xi(z - 1)}$$
$$\sim 2 \int_0^{\infty} \frac{\mathrm{d}\widehat{\Omega}(\xi')}{\mathrm{d}\xi'} \frac{\mathrm{d}\xi'}{\xi' - \xi}. \tag{B.14}$$

Hence, the elasticity equation (20) for a field point close to the crack edge degenerates to

$$\Pi_s(\xi) = \frac{1}{4\pi} \int_0^{\infty} \frac{\mathrm{d}\Omega_s(\xi')}{\mathrm{d}\xi'} \frac{\mathrm{d}\xi'}{\xi - \xi'}. \tag{B.15}$$

B.2. Lubrication

Consider first Poiseuille's law (4) expressed in dimensionless form as

$$\boldsymbol{\Psi} = -\Omega^3 \nabla \Pi, \tag{B.16}$$

where we have assumed the far-field stress to be uniform at the scale at which the asymptotic analysis is carried out. In the vicinity of the crack front, $\xi \to 0$, $\eta = 0$, the net pressure Π depends only on ξ, according to the elasticity Eq. (4). Hence, near the crack front the Poiseuille law (B.16) simplifies to

$$\Psi_{s\xi}(\xi) = -\Omega_s^3 \frac{d\Pi_s}{d\xi}, \quad \Psi_{s\eta} = 0, \quad \xi \ll 1. \tag{B.17}$$

Thus the asymptotic functions $\Psi_{s\xi}$, Π_s, and Ω_s depend only on ξ, near the crack front $\mathscr{C}$. Also, it is convenient to use the modulus of the flux vector $\Psi_s = -\Psi_{s\xi}$ in the asymptotic form of the lubrication equations.

Consider next the volume conservation law (5) without a source term. Acknowledging now that the front is moving at a normal velocity $-v$, parallel to ξ, and thus that the coordinate ξ is moving at velocity v, we can rewrite (5) near the crack front as

$$\frac{D\Omega_s}{D\tau} + v\frac{\partial \Omega_s}{\partial \xi} - \frac{d\Psi_s}{d\xi} + \sqrt{\frac{v}{\xi}} = 0, \quad \xi \to 0, \tag{B.18}$$

where we have taken advantage of the asymptotic form of the solution, and noting that $\partial/\partial\tau - v\partial/\partial\xi = D/D\tau$ denotes the time derivative in the moving coordinate system ξ. Also, we have used the fact that $\tau - \tau_0(\xi) \sim \xi/v$ as $\xi \to 0$.

Since asymptotic considerations of the elasticity Eq. (B.15) indicate that [57]

$$\Omega_s \sim \xi^\alpha, \quad 0 < \alpha < 1, \quad \xi \ll 1, \tag{B.19}$$

in (B.18) the convective term dominates the time derivative as $\xi \to 0$. After integration and taking into account the boundary conditions $\Omega_s(0) = \Psi_s(0) = 0$, near the tip the continuity Eq. (B.18) simplifies to

$$\Psi_s = v\Omega_s + 2\sqrt{v\xi}, \quad \xi \ll 1. \tag{B.20}$$

Appendix C. Analytic solutions for radial fractures

For convenience in this appendix, we summarize four analytical solutions that are available for a radial hydraulic fracture. We will make reference to the $M\widetilde{M}K\widetilde{K}$ parameter space introduced in the main text and shown in Fig. 2.

The first solution (Section C.1) is not restricted, however, to fluid-driven fractures, as it pertains to a radial fracture subjected to a far-field tensile stress and a uniform pressure [52]. However this solution can also be interpreted as the K-vertex solution ($\mu' = C' = 0$).

The solution at the M-vertex is summarized in Section C.2 [54]. This similarity solution can either be interpreted as the solution for a fracture propagating in a medium characterized by $K' = C' = 0$, or as the early time solution if $K' \neq 0$ and/or $C' \neq 0$.

The (zero efficiency) similarity solution at the $\widetilde{M}$-vertex is given in Section C.3 [29]. This solution represents the large-time asymptote for a hydraulic fracture propagating in a zero toughness permeable elastic medium.

Finally, the large toughness solution for a radial fracture propagating in an impermeable medium is summarized in Section C.4 [54]. This solution represents a perturbation from the K-vertex, which thus accounts for viscous flow in the fracture (in contrast to the inviscid flow at the K-vertex). The K-vertex solution is retrieved when the dimensionless viscosity $\mathscr{M}$ vanishes.

C.1. Radial dry fracture in a tensile stress field

Consider a radial "dry" fracture in an infinite elastic body, with a far-field uniform tensile stress field σ normal to the fracture plane. The fracture may also be internally pressurized by a uniform pressure p_f. First we introduce the scaling $x = L_*\chi$, $y = L_*\zeta$, $w = W_*\Omega$, $p_f = \sigma_0\Pi_f$, and $\sigma = \sigma_0\varphi(\chi,\zeta)$, where σ_0 is a characteristic stress. We also define the two characteristic lengths, L_* and W_*

$$L_* = \left(\frac{K'}{\sigma_0}\right)^2, \quad W_* = \frac{K'^2}{\sigma_0 E'} \tag{C.1}$$

to scale the spatial coordinates and the crack aperture respectively. Under this scaling, the elasticity Eq. (3) becomes

$$\Pi_f - \varphi(\chi,\zeta) = -\frac{1}{8\pi}\int_{\mathscr{A}} \frac{\Omega(\chi',\zeta')d\mathscr{S}(\chi',\zeta')}{[(\chi'-\chi)^2 + (\zeta'-\zeta)^2]^{3/2}}. \tag{C.2}$$

Assuming a uniform net pressure $\Pi = \Pi_f - 1$ (i.e., $\varphi(\chi,\zeta) = 1$), the opening displacement and fracture volume for a radial crack of radius γ are given by

$$\Omega = \frac{8\Pi\gamma}{\pi}\sqrt{1 - \left(\frac{\rho}{\gamma}\right)^2}, \quad V = \frac{2^4\Pi\gamma^3}{3}, \tag{C.3}$$

where $\rho = \sqrt{\chi^2 + \zeta^2}$.

There exists a critical radius γ_* for which the stress intensity factor K_I is equal to the toughness K_{Ic}; this condition can be expressed as

$$\Omega \sim (\gamma_* - \rho)^{1/2} \quad \text{as} \quad \rho \to \gamma_*. \tag{C.4}$$

For $\gamma < \gamma_*$ the crack does not propagate ($K_I < K_{Ic}$), while for $\gamma > \gamma_*$ the fracture propagates unstably ($K_I > K_{Ic}$). For a uniform net pressure Π, the critical radius γ_* and the corresponding fracture opening are given by

$$\gamma_* = \frac{\pi^2}{2^7\Pi^2}, \quad \Omega = \frac{\pi}{2^4\Pi}\sqrt{1 - \left(\frac{\rho}{\gamma_*}\right)^2}. \tag{C.5}$$

C.2. M-solution

The M-solution $\mathscr{F}_{mo} = \{\gamma(\tau), \Omega(\rho,\tau), \Pi(\rho,\tau)\}$ is given by

$$\gamma = \gamma_{mo}\tau^{4/9}, \quad \Omega = \Omega_{mo}(\rho)\tau^{1/9}, \quad \Pi = \Pi_{mo}(\rho)\tau^{-1/3}, \quad \text{(C.6)}$$

where a first order approximation to the self-similar solution γ_{mo}, $\Omega_{mo}(\rho)$, $\Pi_{mo}(\rho)$ is given by

$$\gamma_{mo} \simeq 0.6955 \quad \text{(C.7)}$$

$$\Omega_{mo} \simeq (C_1 + C_2\rho)(1-\rho)^{2/3} + B_1[(1-\rho^2)^{1/2} - \rho\arccos\rho], \quad \text{(C.8)}$$

$$\Pi_{mo} \simeq A_1\left[\omega_1 - \frac{2}{3(1-\rho)^{1/3}}\right] - B_2\left(\ln\frac{\rho}{2} + 1\right), \quad \text{(C.9)}$$

with $C_1 \simeq 1.034$, $C_2 \simeq 0.6378$, $B_1 \simeq 0.1642$, $A_1 \simeq 0.3581$, $B_2 \simeq 0.09269$, $\omega_1 \simeq 2.479$.

C.3. $\widetilde{M}$-solution

The $\widetilde{M}$-solution $\mathscr{F}_{\tilde{m}o} = \{\gamma(\tau), \Omega(\rho,\tau), \Pi(\rho,\tau)\}$ is given by

$$\gamma = \gamma_{\tilde{m}o}\tau^{1/4}, \quad \Omega = \Omega_{\tilde{m}o}(\rho)\tau^{1/16},$$
$$\Pi = \Pi_{\tilde{m}o}(\rho)\tau^{-3/16}, \quad \text{(C.10)}$$

where a first order approximation to the self-similar solution $\gamma_{\tilde{m}o}$, $\Omega_{\tilde{m}o}(\rho)$, $\Pi_{\tilde{m}o}(\rho)$ is given by

$$\gamma_{\tilde{m}o} = \frac{\sqrt{2}}{\pi}$$
$$\Omega_{\tilde{m}o} = D_1(1-\rho^2)^{3/2} + D_2\left(\sqrt{1-\rho^2} - \rho\arccos\rho\right)$$
$$+ D_3\sqrt{1-\rho^2}\left[4 - \int_0^1 {}_2F_1\left(\frac{3}{8}, 1, \frac{3}{2}; (1-\rho^2)s^2 + \rho^2\right)ds\right],$$
$$\Pi_{\tilde{m}o} = D_4[4 - (1-\rho^2)^{-3/8}] - D_5[3(2\rho^2 - 1) - 1]$$
$$+ D_6\left[\log\left(\frac{2}{\rho}\right) - 1\right]$$

$$\text{(C.11)}$$

where $D_1 = 0.05159$, $D_2 = 0.1608$, $D_3 = 0.2976$, $D_4 = 0.2596$, $D_5 = 0.01688$, $D_6 = 0.1403$. Here ${}_2F_1()$ denotes Gauss hypergeometric function.

C.4. Near K-solution

The large toughness solution $\mathscr{F}_k = \{\gamma(\tau), \Omega(\rho,\tau), \Pi(\rho,\tau)\}$ is given by

$$\gamma = \gamma_{ko}\tau^{2/5} + \gamma_{k1},$$
$$\Omega = \Omega_{ko}(\rho)\tau^{1/5} + \Omega_{k1}(\rho)\tau^{-1/5},$$
$$\Pi = \Pi_{ko}\tau^{-1/5} + \Pi_{k1}(\rho)\tau^{-3/5}, \quad \text{(C.12)}$$

where $\gamma_{ko} \simeq 0.8546$, $\gamma_{k1} \simeq -0.7349$, and

$$\Omega_{ko} = \left(\frac{3}{8\pi}\right)^{1/5}(1-\rho^2)^{1/2}, \quad \text{(C.13)}$$

$$\Omega_{k1} = B_k(1-\rho^2)^{1/2} - \frac{8}{3\pi}A_k\gamma_{ko}\left[\left(\ln 2 - \frac{4}{5}\right)\right.$$
$$\left. \times(1-\rho^2)^{1/2} + \rho\arccos\rho - \frac{6}{5}I^*(\rho)\right], \quad \text{(C.14)}$$

$$\Pi_{k1} = \Pi_{k1}^* - A_k\left[\frac{1}{3}\ln\rho - \frac{1}{5}\ln(1-\rho^2)\right], \quad \text{(C.15)}$$

with $\Pi_{k1}^* \simeq 0.6380$, $A_k \simeq 1.709$, $B_k \simeq 0.8264$ and

$$I^*(\rho) = \int_\rho^1 \sqrt{\frac{1-\xi^2}{\xi^2 - \rho^2}}\arcsin\xi\, d\xi. \quad \text{(C.16)}$$

Appendix D. Viscosity-toughness scaling

By setting $\mathscr{G}_k = 1$ (rather than $\mathscr{G}_c = 1$), besides imposing $\mathscr{G}_e = \mathscr{G}_m = \mathscr{G}_v = 1$ for the dimensionless groups defined in (18), leads to the so-called viscosity-toughness scaling where the characteristic quantities are now given by

$$L_* = \frac{Q_0\mu'E'^3}{K'^4}, \quad T_* = \left(\frac{Q_0^3\mu'^5 E'^{13}}{K'^{18}}\right)^{1/2},$$
$$W_* = \left(\frac{Q_0\mu'E'}{K'^2}\right)^{1/2}, \quad P_* = \left(\frac{K'^6}{Q_0\mu'E'^3}\right)^{1/2}. \quad \text{(D.1)}$$

Furthermore, the dimensionless leak-off coefficient $\mathscr{G}_c$ is given by

$$\mathscr{G}_c = C'\left(\frac{Q_0 E'^{11}\mu'^3}{K'^{14}}\right)^{1/4}. \quad \text{(D.2)}$$

Since none of the characteristic quantities depend on the leak-off coefficient, this scaling is appropriate to analyze the limiting case of impermeable rocks ($C' = 0$). The scaling factor V_* for the tip velocity is then given by

$$V_* = \left(\frac{K'^{10}}{Q_0\mu'^3 E'^7}\right)^{1/2}. \quad \text{(D.3)}$$

The scaled tip velocity $v = V/V_*$ corresponds to $v = \lim_{\hat{s}\to 0}\hat{q}/\hat{w}$ when $C' = 0$.

The corresponding viscosity-toughness scaling for the tip asymptotics yields the following tip length scale $\widehat{L}_*$ as well as the characteristic tip opening $\widehat{W}_*$ and pressure $\widehat{P}_*$.

$$\widehat{L}_* = \frac{K'^6}{E'^4\mu'^2 V^2}, \quad \widehat{W}_* = \frac{K'^4}{E'^3\mu'V}, \quad \widehat{P}_* = \frac{E'^2\mu'V}{K'^2}. \quad \text{(D.4)}$$

In the absence of leak-off, the asymptotic tip solution has a universal form $\widehat{\Omega}(\hat{\xi})$ and $\widehat{\Pi}(\hat{\xi})$. Although the complete tip solution has to be computed numerically, its series expansion for small and large $\hat{\xi}$ is known explicitly, see (34) and (35).

The tip asymptote can readily be expressed in terms of $\hat{w}(\hat{s})$ from the relationship between the numerical and the tip scaling,

$$\widehat{\Omega} = \frac{W_*}{\widehat{W}_*}\Omega, \quad \hat{\xi} = \frac{L_*}{\widehat{L}_*}\xi, \tag{D.5}$$

which according to (D.1) and (D.4) simplifies to

$$\widehat{\Omega} = v\Omega, \quad \hat{\xi} = v^2\xi. \tag{D.6}$$

Thus Ω behaves according to the viscosity asymptote, $\Omega \sim \beta_0 v^{1/3}\xi^{2/3}$ if $\xi \gtrsim \hat{\xi}_m v^{-2}$, but according to the toughness asymptote $\Omega \sim \xi^{1/2}$ if $\xi \lesssim \hat{\xi}_k v^{-2}$. Obviously, the relevance of either limiting asymptotic behaviour as far as the global solution is concerned depends on the comparison of the length $\hat{\xi}_m v^{-2}$ or $\hat{\xi}_k v^{-2}$ with the fracture characteristic dimension $\gamma = L/L_*$. For example, if $\hat{\xi}_m v^{-2}$ is comparable to $\varepsilon\gamma$ where ε is a small number of order $\mathrm{O}(10^{-2} \sim 10^{-1})$, the tip is locally dominated by the viscosity asymptote; however if $\hat{\xi}_k v^{-2}$ is comparable to $\varepsilon\gamma$ then the tip behaves, at the global scale, according to the LEFM asymptote. As discussed in the main text, our reference length for the application of the tip asymptote will be the characteristic dimension Δs of a grid element and the asymptote will be imposed in a weak form, via the volume.

References

[1] D.A. Spence, D.L. Turcotte, Magma-driven propagation crack, J. Geophys. Res. 90 (1985) 575–580.

[2] J.R. Lister, R.C. Kerr, Fluid-mechanical models of crack propagation and their application to magma transport in dykes, J. Geophys. Res. (1991) 10049–10077.

[3] A.M. Rubin, Propagation of magma-filled cracks, Ann. Rev. Earth Planet. Sci. 23 (1995) 287–336.

[4] D.D. Pollard, G. Hozlhausen, On the mechanical interaction between a fluid-filled fracture and the earth's surface, Tectonophysics 53 (1979) 27–57.

[5] Y. Fialko, On origin of near-axis volcanism and faulting at fast spreading mid-ocean ridges, Earth Planet. Sci. Lett. 190 (2001) 31–39.

[6] V. Slowik, V.E. Saouma, Water pressure in propagating concrete cracks, ASCE J. Struct. Engrg. 126 (2) (2000) 235–242.

[7] G. Bolzon, G. Cochetti, Direct assessment of structural resistance against pressurized fracture, Int. J. Numer. Anal. Methods Geomech. 27 (2003) 353–378.

[8] A.D.M. Penman, The failure of the Teton dam, Ground Engrg. 10 (6) (1977) 18–27.

[9] U. Frank, N. Barkley, Remediation of low permeability subsurface formations by fracturing enhancements of soil vapor extraction, J. Hazard. Mater. 40 (2005) 191–201.

[10] L.C. Murdoch, Mechanical analysis of idealized shallow hydraulic fracture, J. Geotech. Geoenviron. 128 (6) (2002) 488–495.

[11] L.C. Murdoch, W.W. Slack, Forms of hydraulic fractures in shallow fine-grained formations, J. Geotech. Geoenviron. 128 (6) (2002) 479–487.

[12] A.S. Abou-Sayed, D.E. Andrews, I.M. Buhidma, Evaluation of oily waste injection below the permafrost in Prudhoe Bay field, in: Proceedings of the California Regional Meetings, Bakersfield, CA, Society of Petroleum Engineers, Richardson, TX, 1989, pp. 129–142.

[13] A.S. Abou-Sayed, Safe injection pressures for disposing of liquid wastes: a case study for deep well injection (SPE/ISRM-28236), in: Balkema (Ed.), Proceedings of the Second SPE/ISRM Rock Mechanics in Petroleum Engineering, 1994, pp. 769–776.

[14] C. Young, Controlled-foam injection for hard rock excavation, Rock Mechanics for Industry, Proceedings of 37th US Rock Mechanics Symposium, Vail, Colorado, vol. 1, Balkema, Rotterdam, 1999, pp. 115–122.

[15] R.G. Jeffrey, K.W. Mills, Hydraulic fracturing applied to inducing longwall coal mine goaf falls, in: Pacific Rocks 2000, Balkema, Rotterdam, 2000, pp. 423–430.

[16] A. van As, R.G. Jeffrey, Caving induced by hydraulic fracturing at Northparkes mines, in: Pacific Rocks 2000, Balkema, Rotterdam, 2000, pp. 353–360.

[17] J.L. Gidley, S.A. Holditch, D.E. Nierode, R.W. Veatch (Eds.), Recent Advances in Hydraulic Fracturing, SPE Monograph Series, vol. 12, Society of Petroleum Engineers, Richardson TX, 1989.

[18] P. Valkó, M.J. Economides, Hydraulic Fracture Mechanics, John Wiley & Sons, Chichester UK, 1995.

[19] M.J. Economides, K.G. Nolte (Eds.), Reservoir Stimulation, 3rd ed., John Wiley & Sons, Chichester, UK, 2000.

[20] R.J. Clifton, A.S. Abou-Sayed, On the computation of the three-dimensional geometry of hydraulic fractures, in: Proceedings of the SPE Symposium on Low Permeability Gas Reservoirs, Denver, Richardson TX, SPE 7943, Society of Petroleum Engineers, 1979, pp. 307–313.

[21] R.J. Clifton, Three-dimensional fracture-propagation models, in: J.L. Gidley, S.A. Holditch, D.E. Nierode, R.W. Veatch (Eds.), Recent Advances in Hydraulic Fracturing – SPE Monographs, vol. 12, Society of Petroleum Engineers, 1989, pp. 95–108.

[22] A.A. Lacey, J.R. Ockendon, A.B. Tayler, Waiting-time solutions of a nonlinear diffusion equation, SIAM J. Appl. Math. 42 (6) (1982) 1252–1264.

[23] L.J. Bridge, Computational Interface Capturing Methods for Phase Change in Porous Media, Ph.D. Thesis, The University Of British Columbia, November 2006.

[24] D.I. Garagash, E. Detournay, The tip region of a fluid-driven fracture in an elastic medium, ASME J. Appl. Mech. 67 (2000) 183–192.

[25] E. Detournay, J.I. Adachi, D.I. Garagash, Asymptotic and interme-diate asymptotic behavior near the tip of a fluid-driven fracture propagating in a permeable elastic medium, in: A.V. Dyskin, X. Hu, E. Sahouryeh (Eds.), Structural Integrity and Fracture, Swets & Zeitlinger, Liss, The Netherlands, 2002, pp. 9–18.

[26] D.I. Garagash, E. Detournay, Plane-strain propagation of a fluid-driven fracture: small toughness solution, ASME J. Appl. Mech. 72 (November) (2005) 916–928.

[27] S.L. Mitchell, R. Kuske, A.P. Peirce, An asymptotic framework for the analysis of hydraulic fractures: the impermeable case, ASME J. Appl. Mech. 74 (2) (2007) 365–372.

[28] J.I. Adachi, E. Detournay, Plane-strain propagation of a fluid-driven fracture in a permeable medium, Engrg. Fract. Mech., accepted for publication.

[29] M.V. Madyarova, E. Detournay, Fluid-driven penny-shaped fracture in permeable rock, Int. J. Numer. Anal. Methods Geomech., in preparation.

[30] A.P. Peirce, E. Siebrits, The scaled flexibility matrix method for the efficient solution of boundary value problems in 2D and 3D layered elastic media, Computer Methods Appl. Mech. Engrg. 190 (2001) 5935–5956.

[31] A.P. Peirce, E. Siebrits, Uniform asymptotic approximations for accurate modeling of cracks in layered elastic media, Int. J. Fract. 110 (2001) 205–239.

[32] E. Siebrits, A.P. Peirce, An efficient multi-layer planar 3D fracture growth algorithm using a fixed mesh approach, Int. J. Numer. Methods Engrg. 53 (2002) 691–717.

[33] A.P. Peirce, E. Siebrits, A dual mesh multigrid preconditioner for the efficient solution of hydraulically driven fracture problems, Int. J. Numer. Methods Engrg. 63 (2005) 1797–1823.

[34] S. Osher, J.A. Sethian, Fronts propagating with curvature-dependent speed: algorithms based on Hamilton–Jacobi formulations, J. Comput. Phys. 79 (1) (1988) 12–49.

[35] J. Tsitsiklis, Efficient algorithms for globally optimal trajectories, IEEE Trans. Automat. Control 40 (9) (1995) 1528–1538.

[36] J.A. Sethian, A marching level set method for monotonically advancing fronts, Proc. Natl. Acad. Sci. 93 (4) (1996) 1591–1595.

[37] J. Adachi, E. Siebrits, A.P. Peirce, J. Desroches, Computer simulations of hydraulic fractures, Int. J. Rock Mech. Min. Sci. Geomech. Abstr. 44 (2007) 739–757.

[38] M. Stolarska, D.L. Chopp, N. Moes, T. Belytschko, Modeling crack growth by level sets and the extended finite element method, Int. J. Numer. Methods Engrg. 51 (2001) 943–960.

[39] N. Sukumar, D.L. Chopp, B. Moran, Extended finite element method and fast marching method for three dimensional fatigue crack propagation, Engrg. Fract. Mech. 70 (1) (2003) 29–48.

[40] P.C. Paris, M.P. Gomez, W.E. Anderson, A rationale analytic theory of fatigue, Trend Engrg. 13 (1) (1961) 9–14.

[41] E.D. Carter, Optimum fluid characteristics for fracture extension, in: G.C. Howard, C.R. Fast (Eds.), Drilling and Production Practices, American Petroleum Institute, Tulsa, OK, 1957, pp. 261–270.

[42] A.P. Bunger, E. Detournay, Early time solution for a penny-shaped hydraulic fracture, ASCE J. Engrg. Mech. 133 (5) (2007).

[43] S.L. Crouch, A.M. Starfield, Boundary Element Methods in Solid Mechanics, George Allen and Unwin, London, 1983.

[44] D.A. Hills, P.A. Kelly, D.N. Dai, A.M. Korsunsky, Solution of crack problems, The Distributed Dislocation Technique, Solid Mechanics and its Applications, vol. 44, Kluwer Academic Publisher, Dordrecht, 1996.

[45] J.R. Rice, Mathematical analysis in the mechanics of fracture, in: H. Liebowitz (Ed.), Fracture, an Advanced Treatise, vol. II, Academic Press, New York, NY, 1968, pp. 191–311 (Chapter 3).

[46] E. Detournay, D.I. Garagash, Scaling laws for a radial hydraulic fracture propagating in a permeable rock, Proc. Roy. Soc. London, Ser. A, in preparation.

[47] E. Detournay, Propagation regimes of fluid-driven fractures in impermeable rocks, Int. J. Geomech. 4 (1) (2004) 1–11.

[48] D.I. Garagash, E. Detournay, J. Adachi, The tip region of a fluid-driven fracture in a permeable elastic medium, J. Mech. Phys. Solids, in preparation.

[49] A.P. Peirce, Localized Jacobian ILU preconditioners for hydraulic fractures, Int. J. Numer. Methods Engrg. 65 (12) (2006) 1935–1946.

[50] S. Osher, R. Fedkiw, Level set methods and dynamic implicit surfaces, Applied Mathematical Sciences, vol. 153, Springer-Verlag, New York, 2002.

[51] J.A. Sethian, Level Set Methods and Fast Marching Methods: Evolving Interfaces in Computational Geometry Fluid Mechanics Computer Vision and Materials Science, Cambridge University Press, Cambridge, UK, 1999.

[52] I.N. Sneddon, M. Lowengrub, Crack Problems in the Classical Theory of Elasticity, John Wiley & Sons, New York, NY, 1969.

[53] J.A. Ryder, J.A.L. Napier, Error analysis and design of a large-scale tabular mining stress analyzer, in: Proceedings of the 5th International Conference on Numerical Methods in Geomechanics, Nagoya, 1985, pp. 1549–1555.

[54] A.A. Savitski, E. Detournay, Propagation of a fluid-driven penny-shaped fracture in an impermeable rock: asymptotic solutions, Int. J. Solids Struct. 39 (26) (2002) 6311–6337.

[55] D.A. Spence, P.W. Sharp, D.L. Turcotte, Buoyancy-driven crack propagation: a mechanism for magma migration, J. Fluid Mech. 174 (1987) 135–153.

[56] J.R. Lister, Buoyancy-driven fluid fracture: the effects of material toughness and of low-viscosity precursors, J. Fluid Mech. 210 (1990) 263–280.

[57] M.F. Kanninen, C.H. Popelar, Advanced fracture mechanics, The Oxford Engineering Science Series, vol. 15, Oxford University Press, Oxford UK, 1985.